Growth and Characterization of Mid-Infrared Phosphide-Based Semiconductor Diode Lasers

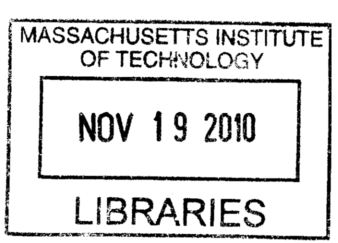
ARCHIVES
MASSACHUSETTS INSTITUTE OF TECHNOLOGY
NOV 19 2010
LIBRARIES

by

Pei-Chun Chi

B.S. Materials Science and Engineering
National Tsing Hua University, Taiwan, 2006

Submitted to the Department of Materials Science and Engineering in partial fulfillment of the requirements for the degree of

Master of Science in Materials Science and Engineering

at the

MASSACHUSETTS INSTITUTE OF TECHNOLOGY

September 2010

© Massachusetts Institute of Technology 2010. All rights reserved.

Author ....
Pei-Chun Chi
Department of Materials Science and Engineering
August 13, 2010

Certified by ....
Leslie A. Kolodziejski
Professor of Electrical Engineering and Computer Science
Thesis Supervisor

Certified by ....
Silvija Gradečak
Assistant Professor of Materials Science and Engineering
Thesis Supervisor

Accepted by ....
Christopher Schuh
Chair, Departmental Committee on Graduate Students

Growth and Characterization of Mid-Infrared Phosphide-Based Semiconductor Diode Lasers

by

Pei-Chun Chi

Submitted to the Department of Materials Science and Engineering
on August 13, 2010, in partial fulfillment of the
requirements for the degree of
Master of Science in Materials Science and Engineering

Abstract

A diode laser emitting at mid-infrared wavelength (2∼5 μm) is an ideal light source for petrochemical or industrial-important gas sensing. Antimony-based III-V compound semiconductor material is the most prominent pseudomorphic epitaxy candidate for this application. However, phosphide-based material not only has the potential to reach this wavelength utilizing a strained active region but also takes the advantage of sophisticated material study from telecommunication technology.

This thesis presents the realization of a 1.97 μm emission ridge waveguide laser in design, fabrication, and characterization phases. $In_{0.85}Ga_{0.15}As/Al_{0.1}In_{0.48}Ga_{0.42}As$ strained multiple quantum wells structures have being built on InP substrates. Structural, optical, and electrical properties of the material have being tested and summarized.

Thesis Supervisor: Leslie A. Kolodziejski
Title: Professor of Electrical Engineering and Computer Science

Thesis Supervisor: Silvija Gradečak
Title: Assistant Professor of Materials Science and Engineering

Acknowledgments

I would like to give my first gratitude to Leslie, my advisor. To me, she is not only a professor who navigates our group, but also an extraordinary mentor who guides me through this challenging period. She always gives me confidence and optimistic opinions, without which I could never finish this work.

Next, I thank Dr. Gale Petrich for enlightening me to the world of MBE. He is a knowledgeable and patient teacher who explains every bolts and nuts of the technique to me. I am very blessed to have Gale always being there for my instantaneous difficulties. I see him a safety net as well as a valuable researcher in our group.

And then, I would like to acknowledge all the research partners from KACST. Dr. Hamad, Dr. Salhi, Abdullah, and Ahmad. Special thank to Dr. Salhi, for his inspiring research and living spirit that I still admire as a role model. I will always remember the time we shared in the PL and optics lab, where I saw the first laser emission in my life.

My very dear group mates: Sheila, Ta-Ming, Orit, and Mohammad, thank you for being true friends and also my consultants in any questions.

Cordial thank to professor Silvija Gradecak, who is my thesis reader in Materials Science Department. Your care and prompt email reply efficiently charge my working power.

Finally I thank my family members, especially my parents. Thank you for giving me so much freedom to do what I want, and nourish my soul in every possible way. You are the best that I could ever ask for.

Thank you Alan, for simply being there waiting and listening.

Thank you, all the machines and equipments I had used in my work. No matter you are a ranch or a MBE, I deeply thank you for reminding me that always be a humble, honest, and courageous person.

Cambridge, 2010

PC Amy Chi

Contents

1 Introduction **15**

1.1 Motivation for Long Wavelength 15

1.2 Challenges in Building MIR Laser 16

1.2.1 MBE Growth 16

1.2.2 Nonradiative Recombination and Threshold 17

1.3 Thesis Overview 20

2 Laser Design and Simulation **23**

2.1 2 μm Strained InGaAs/InP Quantum Well Laser 23

2.2 Laser Structure and Optical Simulation 24

3 Material Growth **29**

3.1 Molecular Beam Epitaxy (MBE) 29

3.2 Growth Condition 30

4 Material Characterization **33**

4.1 Triple Axis XRAY Diffraction 33

4.1.1 High Resolution X-Ray Diffractometer (HRXRD) Set Up . . . 33

4.1.2 Result and Discussion 35

4.2 Photoluminescence (PL) 40

4.2.1 PL Set Up 40

4.2.2 Wet Etch for Laser Structure 41

4.2.3 Result and Discussion 41

4.3 Electroluminescence (EL) 44
4.3.1 Electroluminescence Set Up 44
4.3.2 Testing Materials Preparation 44
4.3.3 Result and Discussion 46

5 Device Characterization **49**
5.1 Device Fabrication 49
5.2 Laser Characterization 50
5.3 Result and Discussion 52
5.3.1 L-I Measurement 52
5.3.2 Thermal Resistance Measurement 61

6 Conclusion and Future Work **65**
6.1 Antimony-Based Material System 65
6.1.1 2.3 μm Antimonide Diode Laser for Photo Acoustic Spectrometry (PAS) 69
6.1.2 Photonic Crystal Tunable Laser 70
6.2 Extension to Longer Wavelength-Dilute Nitrogen Mateirals 71

A Sample ID **73**

B Refractive Index **83**

C L-I-V **85**

List of Figures

1-1 SRH, surface/interface, and Auger recombination process.[1] R_{srh}, $R_{s,i}$, and R_a are the nonradiative recombination rate for Shockley-Reed-Hall, surface and interface, and Auger mechanism. 18

1-2 CHSH Auger recombination process. Filled and hollow circles are the electrons and the holes, respectively, involved in this nonradiative recombination process.[2] 19

2-1 2 μm emitting laser structure with layer content, individual layer thickness, and doping level. 25

2-2 Optiwave simulation of the fundamental optical mode of an InGaAlAs/InP ridge laser (left) and the refractive index profile (right) for different ridge widths: (a) 2 μm, (b) 5 μm, and (c) 10 μm. The x and y coordinates denote the spacial dimension of a ridge waveguide laser; and the color palettes represent the mode intensity (left) and the refractive index (right). 27

3-1 Layout of Veeco GEN200 MBE system. Six cryo pumps (pink), Two turbo molecular pumps (orange), and four scrolling pumps (yellow, one is movable, not shown) are equipped on the system. 31

4-1 Bruker D8 HRXRD instrumental setup. From left to right: X ray source, Goëbel mirror, Ge (022) monochromator, slit, epitaxial sample, slit, Ge (022) monochromator, detector. 34

4-2 (004) $2\theta/\omega$ scan (DAD and TAD) on three laser samples A) VA153 B) VA154 C) VA158. The blue line is the fit to the experimental data shown in the black line. 37

4-3 (Figure 4-2 continued): (004) $2\theta/\omega$ scan (DAD and TAD) on three laser samples D) VA159 E) VA162 F) VA163. The blue line is the fit to the experimental data shown in the black line. 38

4-4 Both the (004) $2\theta/\omega$ and (000) XRR on two PL samples A) VA156 B) VA161. 39

4-5 Block diagram of photoluminescence setup used to characterize thin films. 40

4-6 Compilation of PL results from numerous samples after wet etch (laser structures only) 42

4-7 PL emission wavelength (black rectangles) and lattice mismatch (blue inverted triangles) in the samples. 43

4-8 Block diagram of electroluminescent set up used in this experiment. . 44

4-9 EL spectra for broad area devices: A) VA153, B) VA154, C) VA158, D) VA159, E) VA162A and VA162B (A and B denote differnet devices made out of the same epi film). The measurement is obtained under pulsed driving conditions: 100 ns pulse width, comparable injection current, and various duty cycle (DC%) are labeled in each subfigures. 47

5-1 Cross-sectional SEM photograph of a ridge-stripe laser fabricated by Covega. 50

5-2 Power-current (L-I) testing set up used in the experiment. 51

5-3 Comparison between Covega's measurement (red squares) and the measurement done in this work (blue squares). The blue triangles are the result of the multiplication of a correction factor of 2 on the measured data in this work. 51

5-4 Laser VA153 (a) optical power spectrum, (b) L-I curve under pulsed excitation, (c) internal loss and injection efficiency, (d) L-I-V curve under CW excitation. All measurements are at room temperature, epi-side up. 55
5-5 Laser VA154 (a) optical power spectrum, (b) L-I curve under pulsed excitation, (c) internal loss and injection efficiency, (d) L-I-V curve under CW excitation. All measurements are at room temperature, epi-side up. 56
5-6 Laser VA158 (a) optical power spectrum, (b) L-I curve under pulsed excitation, (c) internal loss and injection efficiency, (d) L-I-V curve under CW excitation. All measurements are at room temperature, epi-side up. 57
5-7 Laser VA159 (a) optical power spectrum, (b) internal loss and injection efficiency, (c) L-I-V curve under CW excitation. All measurements are at room temperature, epi-side down. 58
5-8 Laser VA162 (a) optical power spectrum, (b) internal loss and injection efficiency, (c) L-I-V curve under CW excitation. All measurements are at room temperature, epi-side down. 59
5-9 VA153 defects on the surface treated with and without the wet etch. . 60
5-10 Electroluminescence spectrum of VA163 FP laser device. 60
5-11 Thermal resistance measurement for the laser device VA158 mounted epi-side up: a) and b) are devices with 1.0 mm cavity; c) and d) are devices with 1.5 mm cavity. 62
5-12 Thermal resistance measurement for the laser device VA159 mounted epi-side down: a) and b) are devices with 0.5 mm cavity; c) and d) are devices with 1.0 mm cavity; e) and f) are devices with 1.5 mm cavity. 63
5-13 Thermal resistance with different device mounting configurations . . . 64

6-1 A schematic of various band alignments in the laser structures: a) Type I, b) Type II, and c) Type III (broken type II). 67

6-2 Working principal and design schematic of quartz-enhanced Photo-Acoustic Spectroscopy System. 69

List of Tables

4.1 All 8 epitaxial samples with their structures, QW compositions, and QW numbers. 36

4.2 Wet chemical etch solution used to remove contact layer and cladding layer. 41

6.1 MIR laser diodes 68

B.1 Refractive index used for optical mode simulation 83

Chapter 1

Introduction

1.1 Motivation for Long Wavelength

III-V semiconductor diode laser is preferred nowadays rather than gas or solid state laser in a variety of applications mainly because it is more compact, efficient, reliable and potentially inexpensive. In order to maintain room temperature (RT), continuous wave (CW) operation with low threshold current density (J_{th}), several milestones in improving laser performance have been made. Double Heterojunction (DH) defines the active region for carriers; concept of low dimensionality (i.e. quantum well, quantum dash, and quantum dot) shrinks the active region and moves the laser from gain-guided to index-guided. Incorporation of misfit strain in the active region further decreases J_{th} and modifies the band structure to alleviate Auger recombination. Broad waveguide separate confinement region (SCR) minimizes mode overlapping with the doped cladding layers.[3]

Mid-infrared (MIR, 2~5 μm) wavelength laser is not as well studied as near infrared laser, which has commonly been used in telecommunication applications (1.3~1.5 μm) for decades. Moving toward longer wavelength must address different materials of interest and inevitably, faces different challenges. Important applications using MIR lasers could be categorized in the following:

- Many fundamental absorption lines of several crucial trace gases (CH_4, CO_2, CO, HCl, etc. [3]) are situated in the MIR wavelength regime. Tunable diode laser absorption spectroscopy (TDLAS) is suitable for portable low-cost and room temperature (RT) trace pollutants analysis. For this application, laser diodes that operate under RT with a few tens of milliwatt output power, and good spectral purity are required.

- An important atmospheric transmission windows sits around 3.5~4.2 μm [4]. This facilitates infrared countermeasures to protect aircrafts, ships, and other vehicles against heat-seeking missiles. Additionally, optical free space telecommunications applications are applicable in this wavelength range. Higher output power, usually exceeding 1 watt, is required to meet this need.

- Laser surgery and medical diagnoses, such as noninvasive optical blood glucose monitoring, could also benefit from the availability of mid IR light sources.

1.2 Challenges in Building MIR Laser

1.2.1 MBE Growth

A strained heterostructure is an inevitable choice for long wavelength laser using the phosphide-based material system. Existence of miscibility gap in one quaternary alloy along with strain-induced defects between interfaces may be avoided if one performs a careful design prior to growth. Substrate temperature (T_{sub}), growth rate (GR), and V/III flux ratio are the three major parameters contributing to thin film quality. GR needs to be controlled at a low rate to allow ad-atoms to smoothly distribute themselves into one monolayer having uniform coverage. At the same time, GR should also be fast enough to avoid background impurity incorporation. Optimal V/III ratio creates enough overpressure during the growth to prevent the formation of point de-

fects. Excessively high group V overpressure will adversely hinder group III ad-atoms from moving toward energetically favorable sites by decreasing ad-atom mobility, thus activating 3D growth mechanisms. Finally, T_{sub} is the most sensitive parameter to control because it affects all the reactions occuring on an epitaxial surface. T_{sub} should be high to provide enough kinetic energy to ad-atoms, and low enough not to activate interdiffusion. The former reduces surface roughness and the latter inhibits interfacial intermixing. Both of them have to be controlled to avoid interfacial disorder, which commonly degrades device performance by decreasing electron mobility and further altering the engineered bandgap of the device. Individual growth windows for the above parameters could be found after iterative growths. These parameters may be machine-specific because they are based on different temperature- and flux-monitoring techniques. Here T_{sub} was monitored by a thermal couple and diffuse reflectance spectroscopy (DRS); the molecular flux was monitored by beam equivalent pressure ion gauge.

1.2.2 Nonradiative Recombination and Threshold

Threshold current of a laser diode is dictated by non-radiative and radiative (spontaneous emission) processes. Figure 1-1 illustrates three kinds of non-radiative recombination that occur in the smaller bandgap materials.

Shockley-Read-Hall Recombination (SRH)

SRH recombination occurs with the presence of defects and impurities. Structural defects such as vacancies/interstitials lead to dangling bonds. Impurities such as shallow or deep level dopant (oxygen, for instance, especially in Al-containing alloys) create extra energy states inside the forbidden band gap. The SRH recombination lifetime is typically from 1 to 200 ns in antimony-containing material systems.[5]

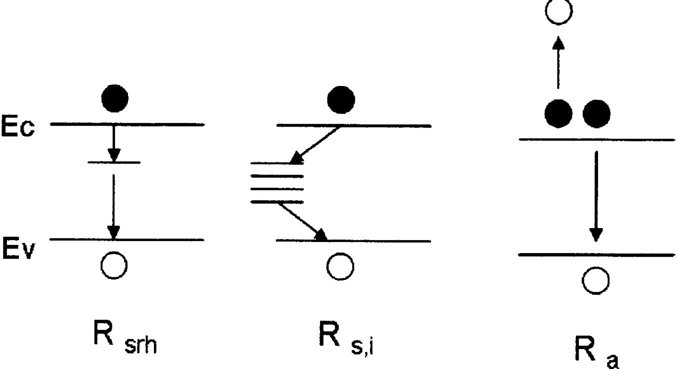

Figure 1-1: SRH, surface/interface, and Auger recombination process.[1] R_{srh}, $R_{s,i}$, and R_a are the nonradiative recombination rate for Shockley-Reed-Hall, surface and interface, and Auger mechanism.

Surface and Interface Recombination

Due to sudden termination of lattice periodicity or change in bond type in different epi layer conjunction, the resulting unsatisfied bonds form minibands inside the band gap. Interface recombination is most severe in reduced dimension structures such as quantum well or quantum dot active regions, accounting for higher interface to volume ratio. Multiple hetero-interfaces and low dimensional active region in a laser structure unavoidably increase the surface and interface recombination rate.

Auger Recombination

Auger recombination is a nonradiative recombination process which accentuates under high carrier density and high temperature environment. An Auger event describes the energy and momentum generated from an electron-hole pair recombination process transfers to a third carrier, resulting a promotion of energy state in this carrier. For a samll band gap material, the energy and momentum conservation is easier to fulfill in this three-particle process. Therefore, Auger recombination becomes a more severe issue in the long wavelength (i.e. small bandgap) material system.

Auger recombination rate could be expressed as:

$$R_a = C(T) \times n^3 \tag{1.1}$$

Where $C(T)$ is proportional to exp(-E_a/k_BT), and

$$E_a = \frac{m_{so}}{m_c + 2m_{hh} - m_{so}}(E_g - \Delta) \tag{1.2}$$

$C(T)$ is the Auger recombination coefficient, calculated to be 5×10^{-29} cm^6/s both in AlGaAsSb/InGaAsSb and InGaAlAs/InP strained QW systems [6][7], n is the carrier density, E_a the thermal activation energy, m_{so}, m_c, m_{hh} are electron effective masses in spin orbit, conduction, and heavy hole band respectively. E_g is the bandgap energy, Δ the spin orbit splitting energy. Figure 1-2 depicts the most prominent Auger transition process, CHSH, in InGaAs strained layers.[2] CHSH process describes an electron sitting at conduction band recombines with a hole at heavy-hole band. The released relaxation energy is then contributing to promote another electron from the split-off band to the heavy-hole band.

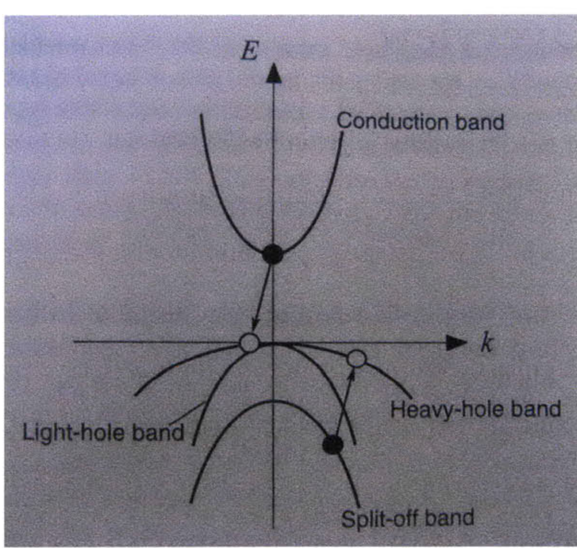

Figure 1-2: CHSH Auger recombination process. Filled and hollow circles are the electrons and the holes, respectively, involved in this nonradiative recombination process.[2]

Obviously Auger lifetime ($\sim 1/R_a$) is affected by carrier density, temperature, band gap, and the curvature of the band. Low bandgap material greatly satisfies the en-

ergy and momentum conservation within this three-particle process. Minimizing the density of final states effectively decreases the Auger recombination rate; this can be achieved by 1) tailoring the separation of energy levels through quantum confinement, and by 2) strain incorporation. In 2), strain alters the valence band curvature and lowers the hole density of states; also the downward-moving valence band maximum increases the energy band gap. These two effects constructively alleviate Auger recombination.

Each of the recombination processes potentially increases the optical loss. Ultimately higher threshold current density is required to achieve lasing. From the above discussion, a well-controlled epitaxial growth on a strain-incorporated active region is the first principal to obtain better device performance.

1.3 Thesis Overview

In this thesis, epitaxial growth, material characterization, device fabrication and characterization of a strained InGaAs/InP multiple quantum wells type-I ridge laser will be described in sequence. The stretegy in this study is to grow a series of "laser structures" and "PL structures" with asymptotic level of indium inside the strained InGaAs quantum well. The difference between the laser structures and the PL structures is that the epitaxial growth fully ceases once completing the InP capping layer, which is on top of the active region. The epitaxial growth, on the other hand, continues on the laser structures with the waveguide, etch stop, cladding, and the top contact. Through material characterization and device testing, the laser and PL structures demonstrate wavelength extension with the increasing indium content. In the future work section, a survey of antimony-based material system which emits at comparable or longer wavelength, but with less strain incorporation, is documented. Also the burgeoning field for longer wavelength emission ($\lambda \geq 3$ μm), namely the addition of dilute nitrogen ($\sim$1%) in antimony-based material system, is introduced in

the last section. A single-mode diode laser emitting near 2.0 μm under RT operation as a light source for photo-acoustic petrochemical sensor application was in collaboration with Professor Rajeev Ram in EECS and Dr. A. Salhi in National Technology Center, King AbdulAziz City for Science and Technology (KACST), Saudi Arabia.

Chapter 2

Laser Design and Simulation

2.1 2 μm Strained InGaAs/InP Quantum Well Laser

The Mid InfraRed (MIR) semiconductor laser device is of great importance in terms of ultra sensitive molecular sensing, since several crucial toxic gas molecules (CH_4, CO_2, CO, and HCl) have their fundamental absorption lines sitting in a spectrum region spanning from 2 to 4 μm. The material of choice for wavelength between 2~3 μm is (AlGaIn)(AsSb) grown on a GaSb substrate. An alternative solution is the use of InGaAs with high indium content as a quantum well and AlGaInAs barriers. This combination allows obtaining an emission wavelength close to 2 μm when grown on an InP substrate.

The sensing application can be achieved by MIR laser diodes operating under room temperature with tens of milliwatt of output power. Previous studies show the phosphide-based material could reach 2 μm emission if more than 1.5% strain is incorporated in the InGaAs quantum wells (QWs). Kuang et al [8] had made a 2.2% strained $In_{0.86}Ga_{0.14}As$-$In_{0.48}Ga_{0.42}Al_{0.1}As$-InP QW diode laser with a 2.2 μm emission wavelength using solid source MBE. This aluminum-cladded design demonstrates higher performance in carrier leakage and maximum operating temperature. In this work, the strained QW concept was adopted to design and grow an aluminum-cladded, phosphide-based laser structure.

2.2 Laser Structure and Optical Simulation

Understanding the energy band structure of a material would lead to fundamental insight of its thermal, carrier transport, and optical properties. For a Type I strained laser, the band offset is of primary importance. Many theoretical efforts have focused on III-V energy band calculation. Here we use the model solid theory, originated by Van de Walle [9] and mathematically implemented by M P C M Krijn [10] to generate the conduction band and valence band offsets of the active region. All the phosphide-related material parameter used in the calculation was tabulated in [11]. Model solid theory allows us to calculate band edge level on an absolute scale, with respect to a common reference level. This reference level is the average electrostatic potential in a semi infinite model solid. The approach facilitates the calculation of the energy level shift due to lattice mismatch strain in the active region. In order to reach 2.2 μm wavelength emission, calculation shows that a minimal 1.5% of strain, or 75% of indium, has to be incorporated in the InGaAs QW. Foutunately, at this alloy composition, thermodynamic calculation confirms that it is out of the miscibility gap. [2] Moreover, Auger recombination rate reaches its minimum at this alloy content. [2] Given the 2 μm target emission wavelength, the QW thickness is determined by 1-D Schrödinger equation for confinement energy calculation. A 8 nm QW thickness is determined after confirming it to the energy balance [12] and mechanical equilibrium [13] critical thickness model.

The second part of the design focuses on the waveguide. The alloy content for waveguide should provide enough band offset for carrier confinement, and at the same time, maintain the large refractive index difference between itself and the InP cladding layer. InGaAlAs quaternary alloy lattice-matched to InP is used to be the waveguide and barrier material. The thickness of the waveguide determines the number of existing optical modes and the optical confinement factor for the laser. Using effective index method, the waveguide thickness is finalized to be 450 nm as a result of sustaining only TE_0 mode. Also we need to minimize the internal loss considering the absorption coefficient and confinement factor in the region where

the optical mode resides. After the active region and waveguide region parameters are determined, the outer cladding thickness and doping profile is finalized and is comparable to that found in the literature.

Commercial design software Harold [14] from Photon Design is used to optimize the device structure further. It is an advanced hetero-structure model which solves self-consistently Poisson's equation, current continuity equations, carrier capture-escape balance equations, and the photon rate equation. Two dimensional (vertical and longitudinal) and pulsed (isothermal) boundary condition was adopted in this calculation. Having this tool, we calculate internal parameters such as internal quantum efficiency and internal loss, L-I characteristics, and optimal number of quantum wells given a particular cavity length.

For an emission wavelength near 2 μm, a complete laser structure will be: a n-type InP substrate, a 500 nm Si-doped InP cladding layer, a 436 nm waveguide consisting of 20 nm lattice-matched $In_{0.48}Ga_{0.42}Al_{0.1}As$ barriers and two 8 nm compressively-strained $In_{0.85}Ga_{0.15}As$ QWs. A 2.2 μm Be-doped InP cladding layer and a 100 nm Be-doped $In_{0.53}Ga_{0.47}As$ contact layer. An etch stop layer made of $In_{0.48}Ga_{0.42}Al_{0.1}As$ is inserted below the p-type InP cladding layer for fabrication convenience. The layer sequence with the corresponding doping is illustrated in Figure 2-1.

p^{++}-$In_{0.53}Ga_{0.47}As$ contact layer	5×10^{19} cm^{-3} (Be doped)	100nm
p-type InP layer	1×10^{18} cm^{-3} (Be doped)	2200nm
p-type $Al_{0.1}Ga_{0.42}In_{0.48}As$ etch stop layer	1×10^{18} cm^{-3} (Be doped)	20nm
p-type InP layer	2×10^{17} cm^{-3} (Be doped)	50nm
$Al_{0.1}Ga_{0.42}In_{0.48}As$ waveguide layer		200nm
$In_{0.85}Ga_{0.15}As$QW		8nm
$Al_{0.1}Ga_{0.42}In_{0.48}As$ barrier		20nm
$In_{0.85}Ga_{0.15}As$ QW		8nm
$Al_{0.1}Ga_{0.42}In_{0.48}As$ waveguide layer		200nm
n-type InP layer	5×10^{17} cm^{-3} (Si doped)	500nm
n-type InP substrate		350μm

Figure 2-1: 2 μm emitting laser structure with layer content, individual layer thickness, and doping level.

A $In_{0.75}Ga_{0.25}As$ quantum well surrounded by $In_{0.48}Ga_{0.42}Al_{0.1}As$ barriers provides a large conduction band and valence band offset (ΔE_c and ΔE_v) . These large values make the structure suitable for high temperature and continuous wave operation. The active region reaches a wavelength of 2 μm with a reasonable amount of strain of 2.11%.

Commercially designed software from Optiwave was used to simulate the optical modes in the proposed structure. This simulation was based on finite-difference Beam Propagation Method (BPM) to calculate the electromagnetic field propagation in the refractive index environment. The refractive index entered in to the simulation and its reference is documented in Appendix B. Note all indices that are used are for 2 μm wavelength. Figure 2-2 shows that the optical mode resides in the high refractive index region under the ridge (2.2 μm depth, various width). Improving lateral optical confinement is observed with increasing ridge width. Optimization is required when considering transversal mode number, optical lateral confinement, and threshold current, in order to fulfill the application purpose.

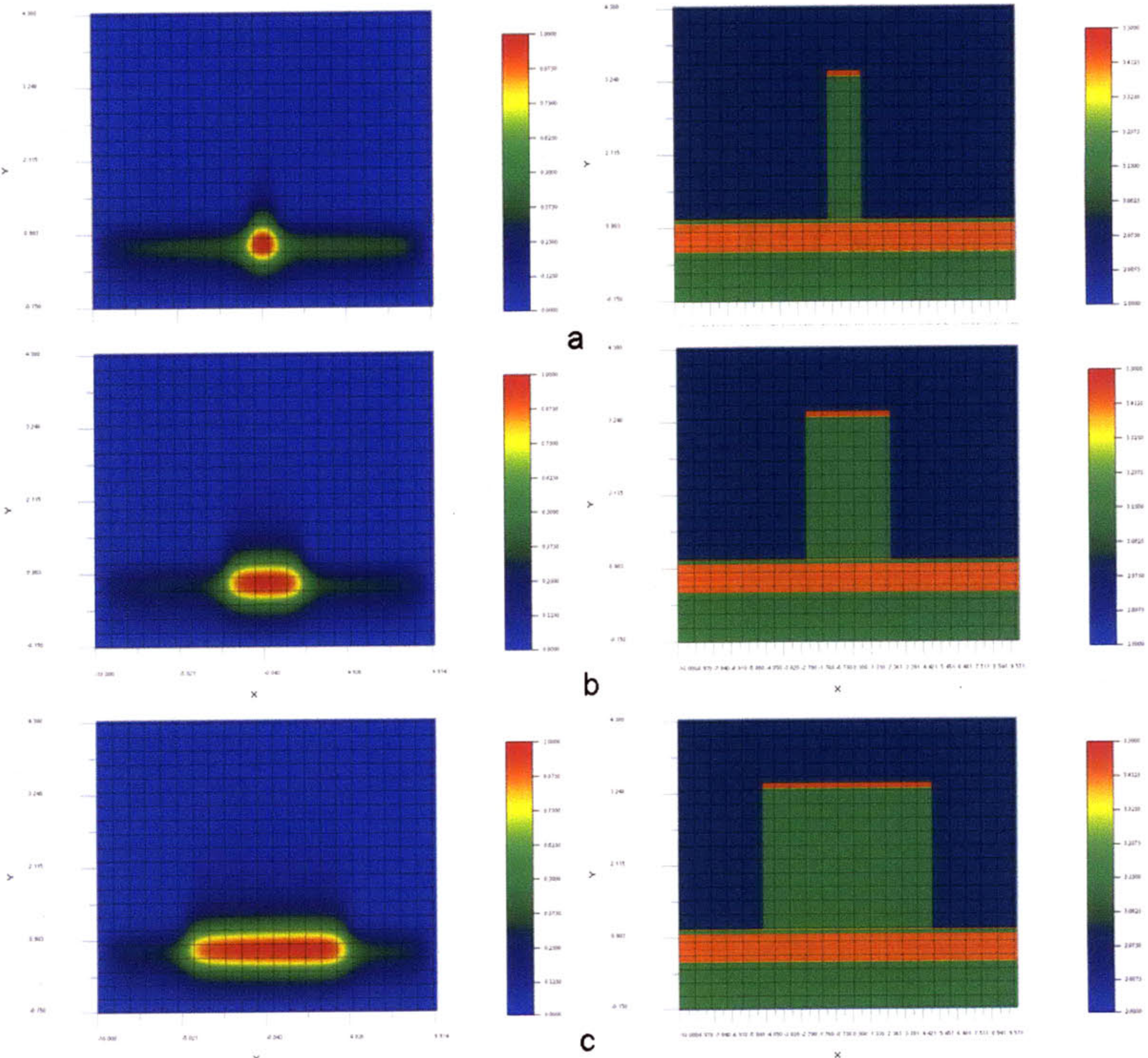

Figure 2-2: Optiwave simulation of the fundamental optical mode of an InGaAlAs/InP ridge laser (left) and the refractive index profile (right) for different ridge widths: (a) 2 μm, (b) 5 μm, and (c) 10 μm. The x and y coordinates denote the spacial dimension of a ridge waveguide laser; and the color palettes represent the mode intensity (left) and the refractive index (right).

Chapter 3

Material Growth

3.1 Molecular Beam Epitaxy (MBE)

Solid source, dual-reactor Veeco GEN200 molecular beam epitaxy system in the Nano Precision Deposition Lab was used to conduct all epitaxial growth in this thesis. MBE is unique in its ultra high vacuum (UHV, $\leq 10^{-9}$ Torr) growth environment, which ensures evaporated group III atoms or group V molecules travel in a line-of-sight trajectory before reaching the vicinity of the substrate. To maintain UHV, this system is equipped with six cryo pumps as primary pumping system; two turbo-molecular pumps for phosphorous operation; and four scrolling pumps as the secondary pumping system that brings the pressure from 760 Torr (1 atm) to 10^{-3} Torr. The specific layout of the Veeco GEN200 is detailed in Figure 3-1. The cryo pump only operates below 10 K and a vacuum of 10^{-3} Torr. A cryo pump causes cryo-condensation of gas species on a series of baffles. In a similar principal, but without moving parts, cryopanelling maintains the reactor body at 77K (liquid nitrogen boiling point) as an auxiliary pumping system which collects condensable gases, particularly H_2O and heavier hydrocarbons. Extensive cryopanelling surrounding the deposition region is an essential design for achieving high quality aluminum-containing films.

The MBE system has two reactors distinguished by their source materials. Reactor A has group III materials: gallium, indium, aluminum; group V materials: arsenic, phosphorous, nitrogen; doping materials: silicon and beryllium; and hydrogen for

regrowth surface cleaning. Reactor B also has all the above with an additional group V material: antimony. Two gallium and two indium cells on each reactor ensure high film quality by minimizing growth hiatus due to cell temperature adjustment. A thermal effusion cell radiatively heats the solid source and the evaporants form a molecular beam. A thermocouple is positioned in contact with the pyrolytic boron nitride crucible, registering the source material temperature, and controls the power to the heater via a proportionalintegralderivative (PID) feedback. Valve cracker is an extended heating zone equipped in all group V cells in order to 1) pyrolyse tetrameric molecules into dimeric molecules, or even monomeric molecules, and 2) control the volatile group V flux through a precision valve opening rather than by controlling source temperature. Utilizing dimeric or monomeric molecules not only supports better film quality [15] but also preserves the quantity of group V materials during growth. Fourteen two-inch wafers or seven three-inch wafers can be loaded into a single reactor in one growth experiment. Only the loading chamber is exposed to atmosphere; wafer transferring inside both reactors is controlled by an automated robot arm.

A substrate heater, attached to the manipulator, radiatively heats the substrate in proximity. Although the temperature in the system is primarily controlled by the thermo-couple, diffuse reflection spectroscopy (DRS) is also used for accurate substrate temperature measurement. The ionization guage is not sensitive enough to measure dopant fluxes but is capable of measuring fluxes down to 10^{-11} Torr.

3.2 Growth Condition

Substrate temperature, growth rate, and V/III ratio were pointed out in Section 1.2.1 to be the most critical growth parameters. These data are documented in Appendix A. Throughout all the growth experiments in this thesis, a nominal substrate temperature between 590∼600°C was used, whereas DRS showed a nonlinear shift of the real temperature, which sits in 487∼508°C. Group III and group V beam equivalent pressure (BEP) were also tabulated in Appendix A. Direct calculation of BEP V/III

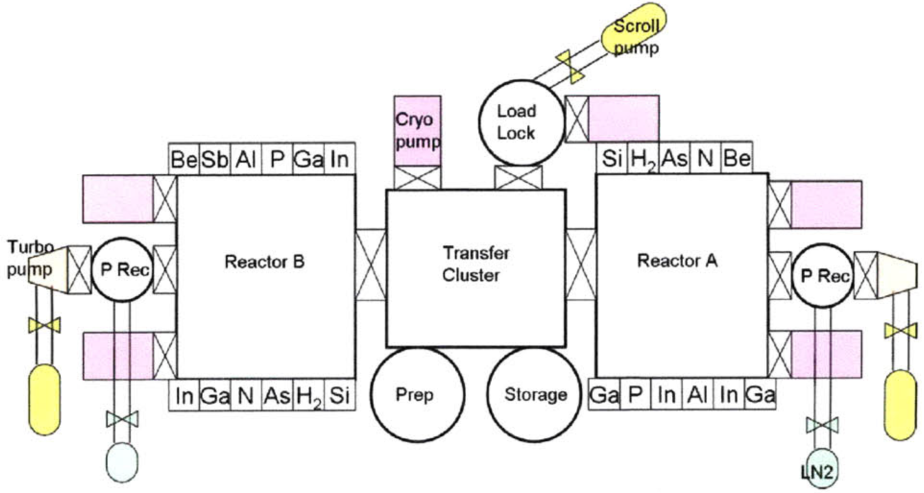

Figure 3-1: Layout of Veeco GEN200 MBE system. Six cryo pumps (pink), Two turbo molecular pumps (orange), and four scrolling pumps (yellow, one is movable, not shown) are equipped on the system.

ratio falls in 19~23. However, caution is required when examining the reports of V/III ratio in literature. Normally the report should specify whether the parameter is V/III BEP ratio or the V/III growth rate ratio. The latter is a common language when reflection high energy electron diffraction (RHEED) is in use. Two curves need to be obtained in the calibration runs: first, the growth rate as a function of group III flux under excess group V overpressure, and second, the growth rate as a function of group V flux under excess group III overpressure. One is able to claim, according to the two curves measured, the V/III growth rate ratio given the group V and group III flux used in the subsequent growth experiment. The numerator is the growth rate on the first curve obtained under limiting group III flux; and the denominator is the growth rate on the second curve obtained under limiting group V flux. Growth under excess group V is adopted in this experiment for it provides better film quality. Arsenic cell base temperature and valve position (in mil, 1 mil=0.001 inch) were also recorded in Appendix A.

Chapter 4

Material Characterization

4.1 Triple Axis XRAY Diffraction

4.1.1 High Resolution X-Ray Diffractometer (HRXRD) Set Up

The Bruker D8 HRXRD is used to analyze all epitaxial samples. It is a triple-axis diffractometer (TAD) consisting of a four-bounce Ge (022) asymmetric beam conditioner (first axis), the sample crystal (second axis), and a receiving three-bounce Ge(022) analyzer crystal (third axis). This configuration gives a 25 arc-seconds beam divergence and a 0.008 degree FWHM on Si (022). It is a versatile characterization tool which allows one to perform high resolution xray diffraction (HRXRD) as well as xray reflectometry (XRR) on a non-lattice matched, simple multilayer thin film stacks.

Ideally this system is able to reach a 5 arc-seconds beam divergence with an alternative four bounce Ge (044) symmetric monochromator. This condition is more appealing to analyze a complicated laser structure consisting of multiple layers. However, the increase of 5 times in resolution is at the expense of signal intensity, which turns out to be three orders of magnitude lower. To further increase the diffraction beam intensity, double axis diffraction (DAD) is also used. In DAD, the analyzer crystal at the receiving end is replaced by a slit. Shown in Figure 4-1 is a generic

diagram of a TAD system used in the measurement. Copper K_α line (λ=1.54 $\AA$) is generated from electron bombardment. The divergent beam then passes through a Goëbel mirror and enters a Ge (022) monochromator. The conditioned (more collimated and spectrally pure) Xray beam reaches the sample after passing through a 0.2 mm slit. The reflected beam then enters a detection system that switchs between a programmable receiving-slit or Ge (022) analyzer crystal.

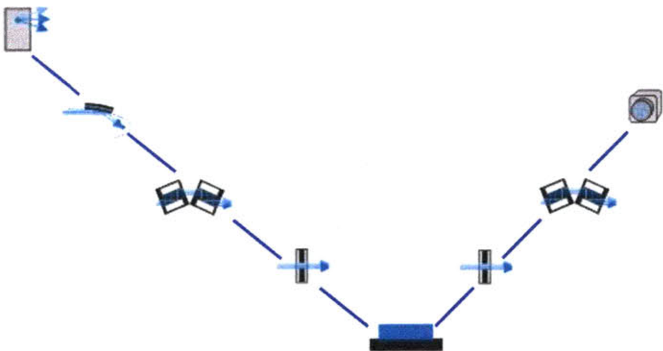

Figure 4-1: Bruker D8 HRXRD instrumental setup. From left to right: X ray source, Goëbel mirror, Ge (022) monochromator, slit, epitaxial sample, slit, Ge (022) monochromator, detector.

A symmetric (004) $2\theta/\omega$ measurement is first performed. By changing the detector position along with the incident beam angle, different (hkl)s contribute to constructive interference; therefore this type of scan is especially sensitive to perpendicular lattice constant (a_z). Usually one spectrum is enough to obtain composition and thickness information through software fitting assuming a simple structure with no lattice plane tilt, strain, relaxation, or surface curvature. The conditions mentioned above complicate the composition analysis and an extra asymmetric (224) or (115) scan should be performed to gather more in-plain lattice, namely a_x and a_y, information if desired. A multiple quantum well laser could be viewed as a superlattice structure embedding in cladding layers. Thickness fringes, satellite peaks, and substrate peak complicate the diffraction pattern with serious interference between each others' scattering amplitudes. Grazing angle (000) X-ray reflection (XRR) measurement is a time-efficient technique performed to improve the fitting accuracy of the data. XRR is used to

measure the density, thickness and roughness of thin layers (20~200 nm). The above information is obtained through critical angle, fringe thickness, and the overall signal decay analysis. LEPTOS [16] is the primary simulation and fitting software for HRXRD used in this thesis. LEPTOS adopts recursion matrix extension to the dynamical diffraction theory, where the multiple scattering processes have been treated exactly. The program models a heterostructure into a stack of parallel atomic planes. The thickness and composition of each plane is varied until the best fit between the simulation and experimental curve is achieved.

4.1.2 Result and Discussion

Table 4-1 shows basic information on all 8 epitaxial samples discussed in this study. All the layer information generated by data fitting could be found in Appendix A. Film thickness, density, alloy composition, residual stress, and roughness of the thin film will be obtained after fitting the experimental data. Figure 4-2 and Figure 4-3 show (004) $2\theta/\omega$ scans on every laser structure. Two graphs are shown for each sample, one with the higher signal intensity and broader scanning range and the other with lower intensity and narrower range. The former is obtained by DAD and the latter TAD. Because (000) XRR is a surface analysis (20~200 nm) technique, the intensity oscillation feature could not be obtained for a complete laser structure because the 2200 nm cladding layer is thicker than the distinction length (XRR for laser structures is not shown here). Figure 4-4 shows both (004) $2\theta/\omega$ scan in DAD and TAD configurations, as well as the (000) XRR spectrum obtained from two PL structures. Sample analyzer in the software is used to generate a convergent fit to the data based on the above scans. The fitting process is configured to use "Genetic Algorithm" first to find a global minimum and then "Levengerg-Marquardt" method continues as a local minimizer for fine tuning the fit to the data.

The most prominent feature in the spectra is the substrate peak around 63.25° (2θ). Toward high angle side, the broader peak with very fine fringes close to 64° (2θ) is attributed to the InGaAs top contact. The existence of this peak verifies a slight tensile strain in the nominally lattice-matched contact layer due to unintentional

Sample	QW Composition	#QW	Structure
VA153	$In_{0.66}GaAs$	2	Laser
VA154	$In_{0.66}GaAs$	3	Laser
VA156	$In_{0.71}GaAs$	2	PL
VA158	$In_{0.71}GaAs$	2	Laser
VA159	$In_{0.71}GaAs$	3	Laser
VA159	$In_{0.76}GaAs$	2	PL
VA162	$In_{0.74}GaAs$	2	Laser
VA163	$In_{0.75}GaAs$	3	Laser

Table 4.1: All 8 epitaxial samples with their structures, QW compositions, and QW numbers.

dilute phosphorous incorporation. The quaternary waveguide layers are very close to lattice-matched condition, and the superlattice nature generates a series of satellite peaks between 63° to 64°, which strongly interfere with the substrate's scattering amplitude. Toward the small angle side, an even broader envelope containing periodic fringes is observed, which then provides the information on the compressively-strained InGaAs quantum well indicating its alloy content and thickness. The position of the envelope maxima moves toward lower angle along with increasing indium content in QWs. Note the diffraction pattern for structures with two QWs is different from that with three QWs. An alternate increase and decrease of fringe maxima is shown in 3 QWs samples because the embedding environment modulates the fringe maxima and period differently.

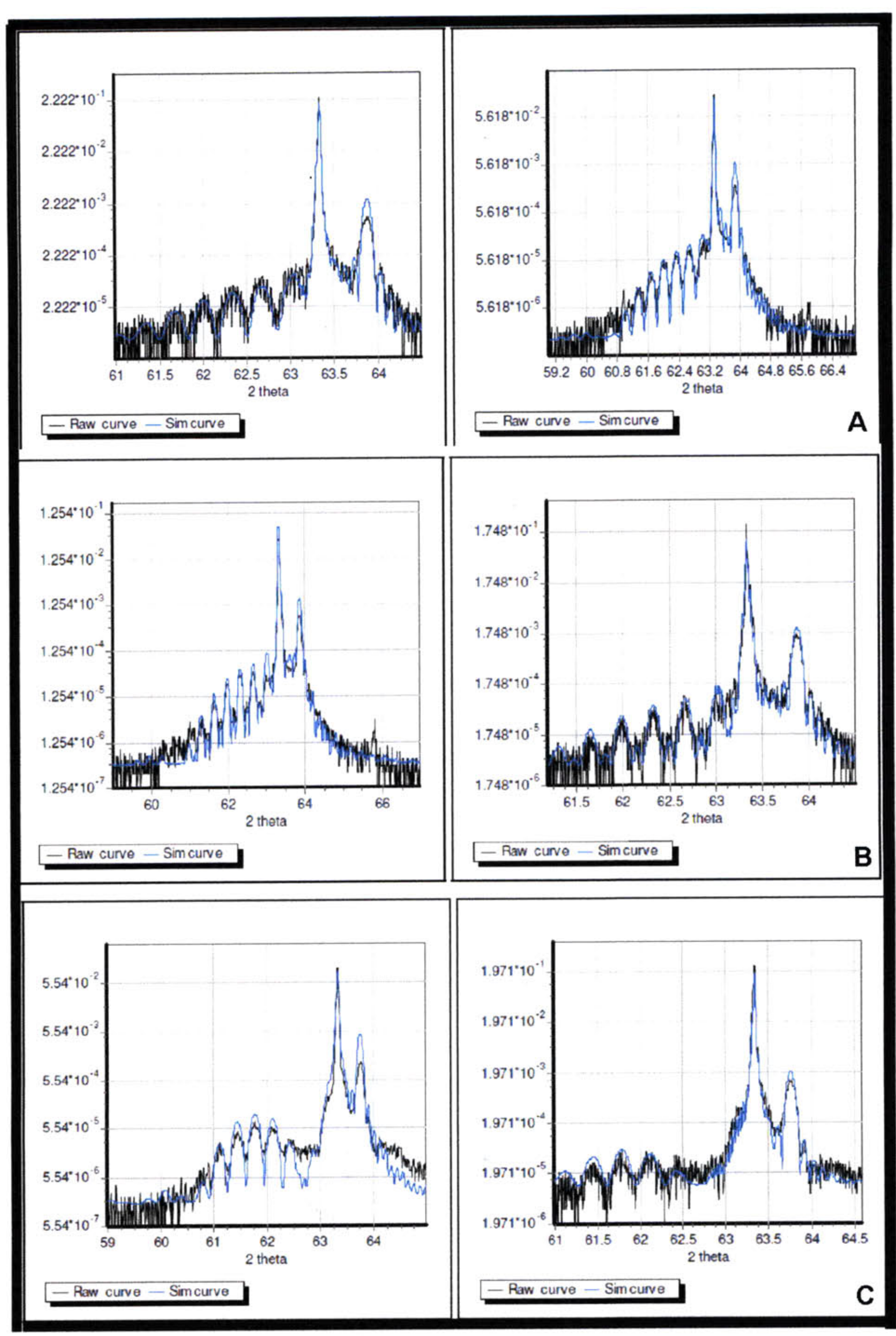

Figure 4-2: (004) $2\theta/\omega$ scan (DAD and TAD) on three laser samples A) VA153 B) VA154 C) VA158. The blue line is the fit to the experimental data shown in the black line.

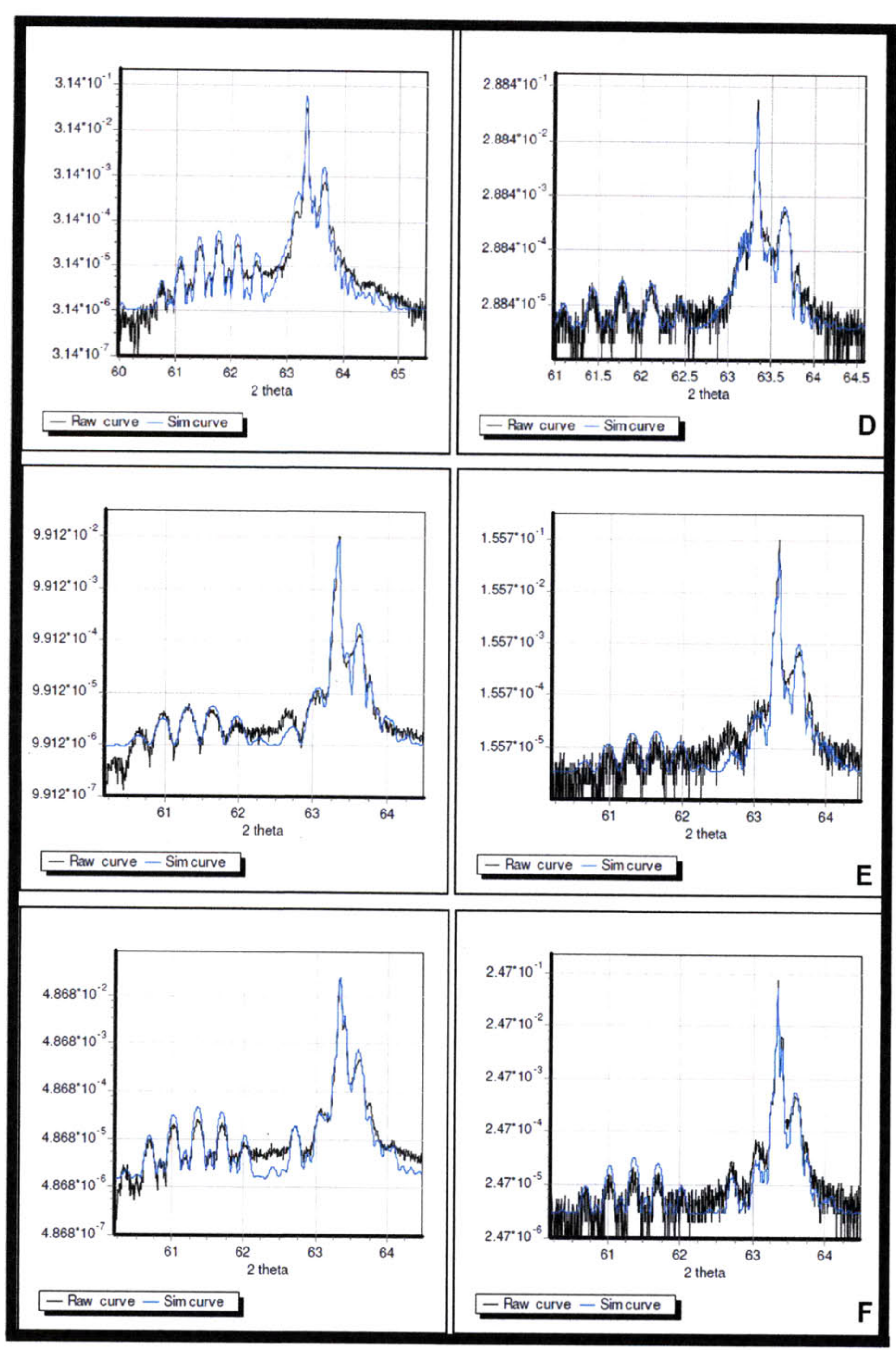

Figure 4-3: (Figure 4-2 continued): (004) $2\theta/\omega$ scan (DAD and TAD) on three laser samples D) VA159 E) VA162 F) VA163. The blue line is the fit to the experimental data shown in the black line.

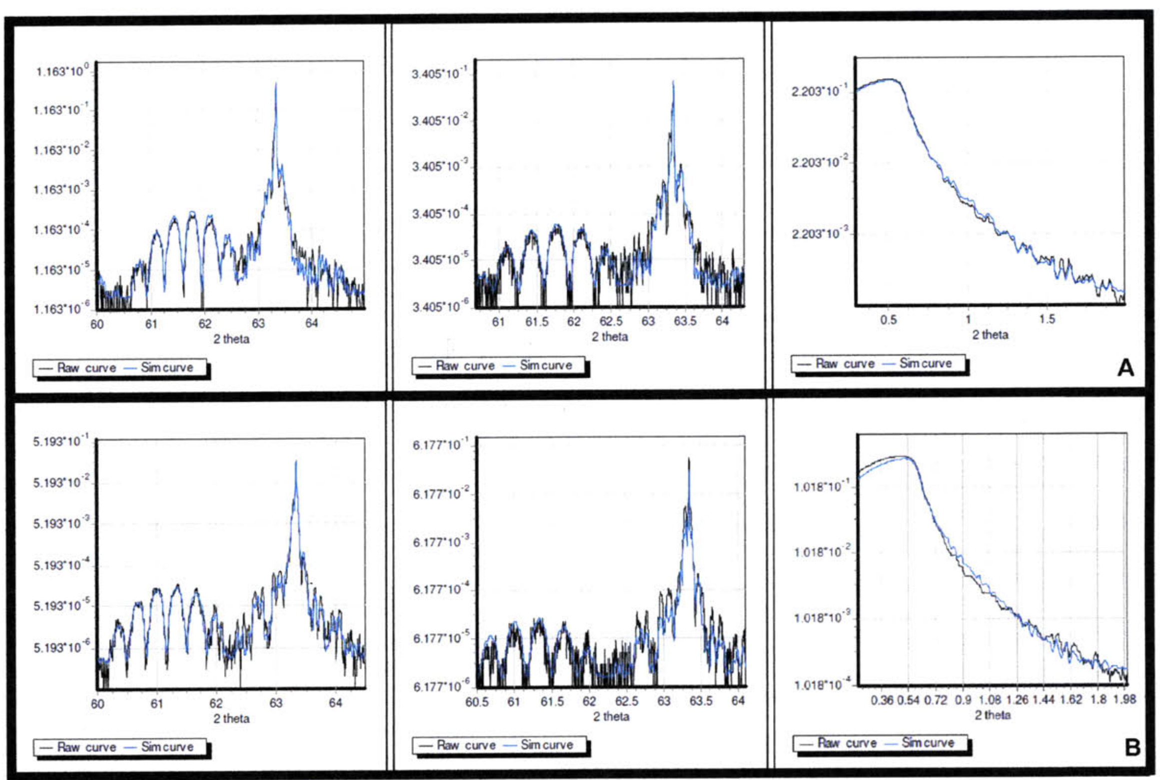

Figure 4-4: Both the (004) $2\theta/\omega$ and (000) XRR on two PL samples A) VA156 B) VA161.

4.2 Photoluminescence (PL)

4.2.1 PL Set Up

Figure 4-5 depicts the existing photoluminescence setup used for optical characterization of the epilayers. A 514.5 nm argon ion laser serves as the photoexcitation source. The laser beam is then routed through a chopper, which is programmed at 534 Hz, in order to increase the signal to noise ratio with the presence of a lock-in amplifier. Subsequently passing through a height adjusting mirror, the laser beam is directed to hit the sample, which is positioned at an angle slightly off from 90°. The sample holder is tilted to reflect the laser beam out of the optical axis. The light emitted by the sample is routed through two focusing lens and then goes into a PbS detector. The detected signal is transferred to a lock-in amplifier . All the samples in this thesis were designed to emit in the MIR wavelength region, therefore grating number three, which allows to scan from 900nm to the longest possible wavelength 2400 nm is in use.

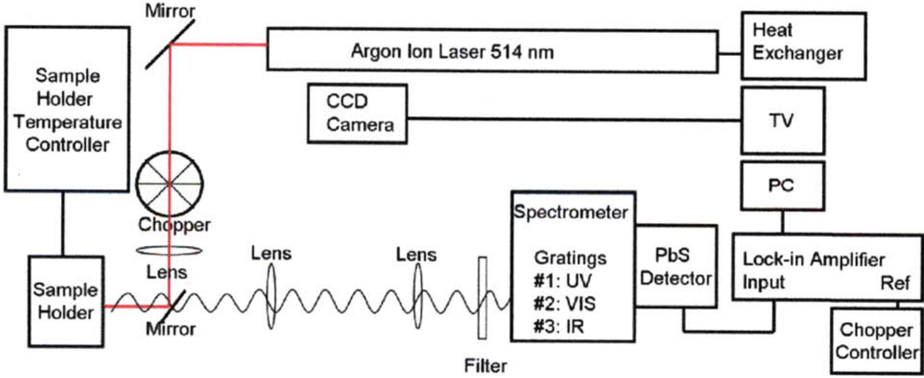

Figure 4-5: Block diagram of photoluminescence setup used to characterize thin films.

All PL measurements are conducted at RT. Sample VA153, VA154, VA158, VA159, VA162, and VA163 are complete laser structures. The sensitivity of the lock-in amplifier is set to be 2 mV for all the laser samples mentioned above. Sample VA156 and VA161 are PL structures, which were measured under 2 mV and 1 mV sensitivity, respectively. Note that the difference between samples designed for PL characterization

and the complete laser structure is that the epitaxial growth stops upon the completion of the waveguide layer in the former case. Incident light can easily penetrate through the thin surface layer with little absorption penalty and reach the active region where radiative recombination takes place. However, with a thick 2.2 μm upper cladding in a complete laser structure, incident light intensity will inevitably decay to a negligible value and only the recombination at the top contact layer is observed. Therefore a wet etch process is introduced prior to the PL characterization of all laser structures.

4.2.2 Wet Etch for Laser Structure

The wet etch process for this specific laser consists of two steps: 1) the removal of the InGaAs contact layer, where an arsenide-based etchant is used; and 2) the removal of the InP cladding layer, where a phosphide-based etchant is used. The chemical solutions that are used are detailed in Table 4-2. All etching processes were carried out at RT, using as-prepared etching solution. Theoretically, the second etching step should stop at the InGaAlAs etch stop layer. However, in some samples, the InP cladding was not thoroughly removed. From the energy band point of view, the underlying etch stop turns into a 20 nm energy well that contributes to an extra emission peak with low intensity.

	Etch Solution	**Reference**
For Arsenide	H_3PO_4:H_2O_2:H_2O = 1:1:3	[17]
For Phosphide	H_3PO_4:HCl:CH_3COOH = 1:1:2	[18]

Table 4.2: Wet chemical etch solution used to remove contact layer and cladding layer.

4.2.3 Result and Discussion

Figure 4-6 is a compilation of the PL results obtained from all the structures grown. PL structures show consistency in emission wavelength with their laser counterparts. Structural information for each sample was documented in Appendix A. It is important to note that the PL structures have higher intensity than similar laser structures

but comparable full-width- half-maximum (FWHM). Although one may attribute the photon loss to the presence of a roughened surface or residual unetched materials, the succeeding cladding growth may also affect the optical integrity of the active region. The growth of the cladding layer is equivalent to a 2 hour annealing event. All samples show FWHM around 40 meV at RT. The broad FWHM implys the crystal quality may need improvement. Also note that the PL intensities from samples with three quantum wells are higher than from samples with two quantum wells due to more radiative recombination taking place in the additional quantum well. Figure 4-7 shows the trend that both PL emission wavelength and lattice-mismatch increase with increasing indium content.

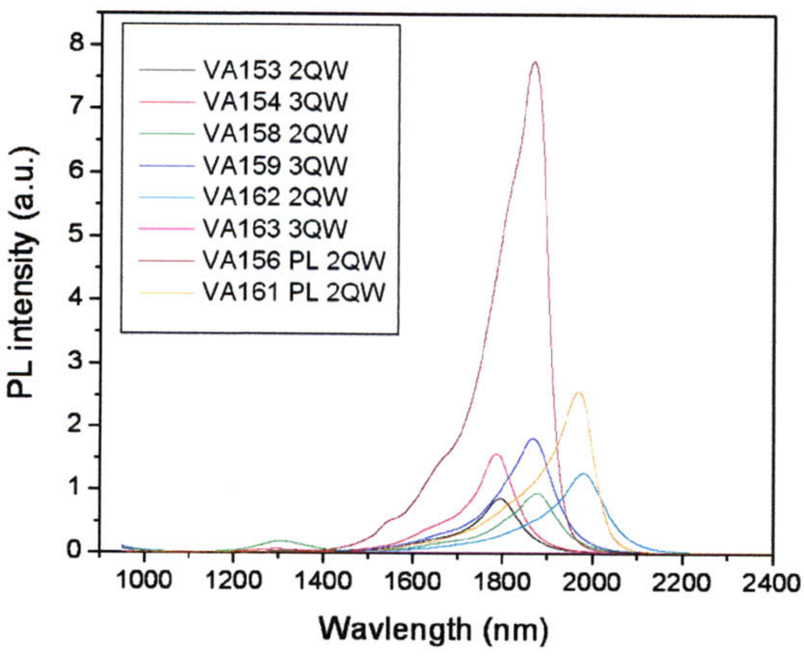

Figure 4-6: Compilation of PL results from numerous samples after wet etch (laser structures only)

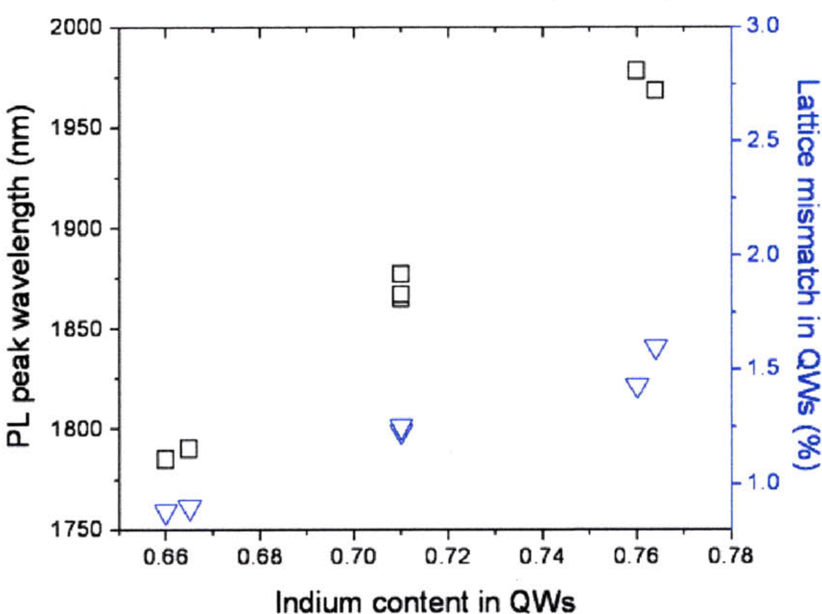

Figure 4-7: PL emission wavelength (black rectangles) and lattice mismatch (blue inverted triangles) in the samples.

4.3 Electroluminescence (EL)

EL is a way to characterize the electrical properties of a laser device once the metal contact is formed. An ohmic contact is required at the metal-semiconductor junction to assure ease of carrier transport without a large resistance. A problematic metal contact not only creates a Schottky barrier but also contribute to Joule heating of the device. With increasing device temperature, higher threshold current will be needed.

This section describe a simple EL test where only the metal evaporation step to form the contact is carried out in the clean room. The devices under characterization are broad-area Fabry-Perot cavities without any ridge waveguide definition.

4.3.1 Electroluminescence Set Up

Figure 4-8 shows the generic scheme for the electroluminescent set up. ILX lightwave LDC-3900 and LDC-3840 modular laser diode controllers are used as continuous and pulsed laser drivers. A broad area Fabry-Perot laser diode is placed on a thermal electric probing stage which maintains room temperature. The luminescence generated from the device is focused by a two-lens (aspheric and objective lens) set of optics that allows XYZ control for fine adjustment and signal maximization. The light signal is then guided by a multimode optical fiber to an optical spectrum analyzer (OSA, YOKOGAWA AQ6375 1200~2400 nm).

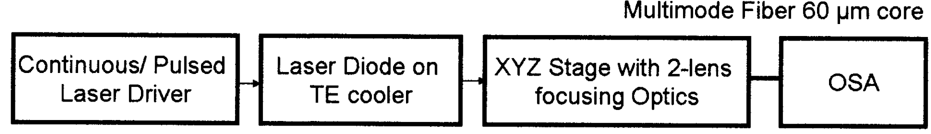

Figure 4-8: Block diagram of electroluminescent set up used in this experiment.

4.3.2 Testing Materials Preparation

All samples are first mechanically thinned to 150 μm and then each cample undergoes the same metallization : Ge 18 nm/Au 30 nm/Ni 20 nm/Au 200 nm as the n-side

metal contact and Ti 30 nm/Pt 20 nm/Au 200 nm as the p-side metal contact, followed by a 30 second, 400°C rapid thermal annealing (RTA) step. A rib-back carbon steel surgical blade is used to cleave the wafer into 1 mm wide long stripes. Inspection under an optical microscope ensures both facets are mechanically perfect, then cleave the stripes into 1 mm×500 μm Fabry-Perot (FP) cavities.

The FP cavity is soldered to a copper block (heat sink) using lead-tin solder or indium foil. First the hotplate is preheated to 250°C and rub the copper block is scraped using sharp blades, in order to remove any surface oxide. The copper block is placed on the hotplate for 5 minute and is then wetted by the lead-tin wire or indium foil on one long side of the copper block. Although containing hazardous material (lead), lead-tin solder is used for all the soldering processes in this thesis because of its superior wetting property. Blades are used to remove excess molten solder material to obtain as thin of a layer as possible. A thin and uniform soldering layer is needed to prevent a short circuit when mounting the FP device. Keeping the hot plate temperature to 155°C will retain a semi-liquid solder.

The following work is all conducted under the optical microscope due to the small size of the FP cavity. Mount the device n-side down with a fine tweezer, and gently adjust the position and angle of each die to be close and perpendicular to the edge of the copper block. Extra care should be taken to avoid facet damage and the creation of a short circuit. Turn off the hotplate, and allow the whole device to cool down with the hotplate at a slow rate, in order to prevent the generation of strain-induced micro-cracks due to thermal quenching.

4.3.3 Result and Discussion

Testing was carried out under both continuous- and pulsed-driving conditions. However, electroluminescence is only observed under pulsed condition. EL spectrum shown in Figure 4-9 are all taken under 100 ns pulse width, with various duty cycles (DC) and current injection. Lasing behavior is defined to have the FWHM of the emission peak narrower than several nanometers. Only VA153, VA154, VA159, and VA162 show lasing behavior whereas VA158 shows amplified spontaneous emission (ASE). VA163 (not shown) has no features.

From the emission wavelength on the optical spectrum analyzer, peak positions shift to longer wavelength with samples containing more indium. Samples tested with the same injection current are prone to lase under lower duty cycle. This is because less self-heating keeps the threshold current low. With increasing duty cycle from pulse (DC 0.5%) to semi-continuous (DC 5%) condition, ASE is observed instead of the defined lasing peak.

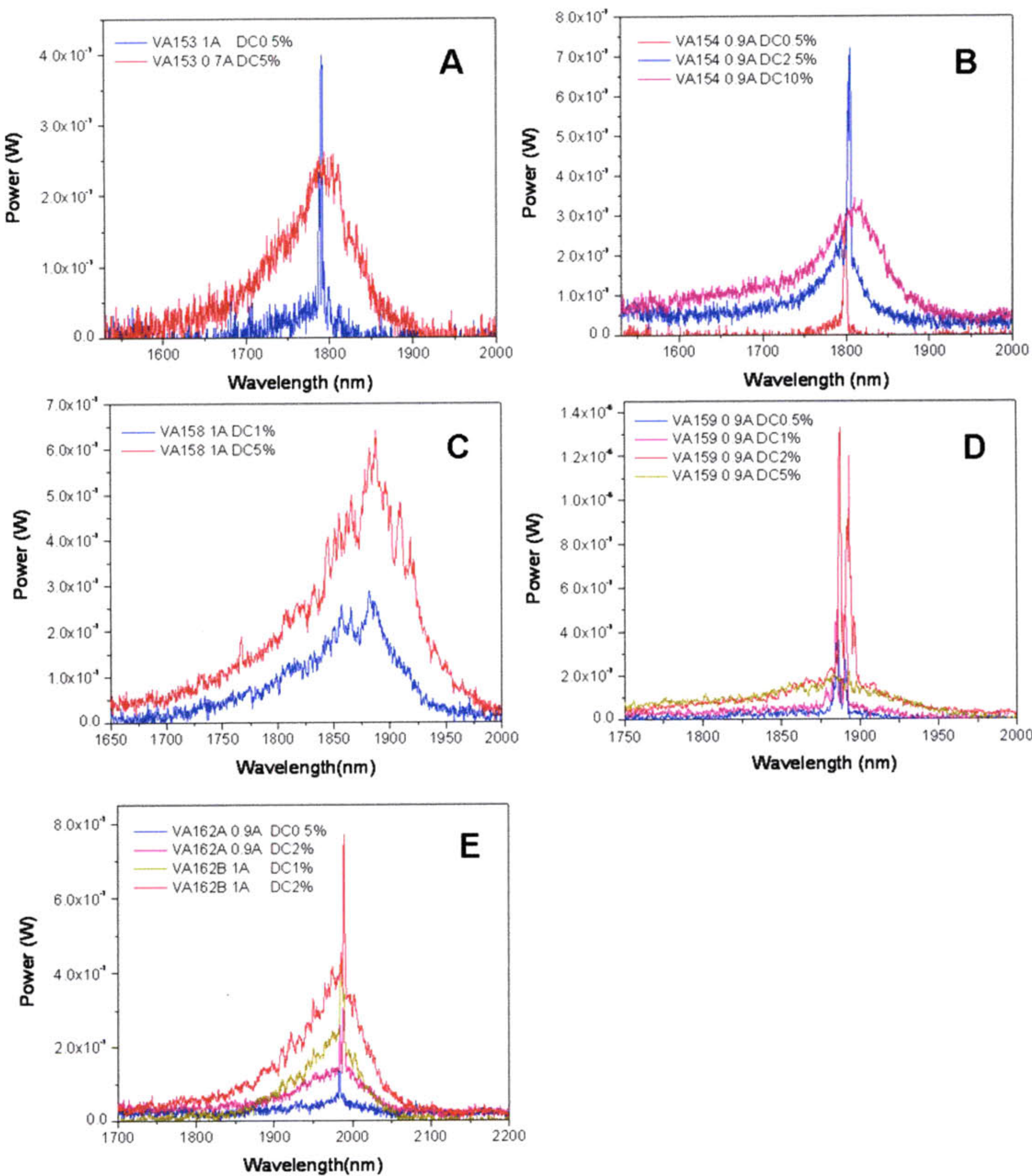

Figure 4-9: EL spectra for broad area devices: A) VA153, B) VA154, C) VA158, D) VA159, E) VA162A and VA162B (A and B denote differnet devices made out of the same epi film). The measurement is obtained under pulsed driving conditions: 100 ns pulse width, comparable injection current, and various duty cycle (DC%) are labeled in each subfigures.

Chapter 5

Device Characterization

5.1 Device Fabrication

Seven ridge-stripe laser samples (VA152, VA153, VA154, VA158, VA159, VA162, VA163) were fabricated by Covega[1]. Back-end processing includes reactive ion etch, spin-on glass, wafer thinning, metal evaporation (back and front side), and laser bar cleaving. The first two steps were performed for current confinement and planarization. P-side metal (Ti/Pt/Au total 930 nm) and n-side metal (Au/Ge/Ni/Pt/Au total 880 nm) were deposited before and after wafer lapping respectively. The processed wafer is then cleaved into 1.5 cm bars with 20 laser dies on each bar. Figure 5-1 shows the scanning electron microscope cross-sectional view of the ridge laser. Each sample has two identical sets of laser bars in various cavity lengths (0.5 mm, 1 mm, 1.5 mm). The L-I (light intensity vs. injection current) testing results from devices with different cavity lengths allow one to obtain internal parameters such as internal loss and current injection efficiency. The corresponding principals and processes are detailed in the following section.

[1]Thorlabs acquired Covega Technlogy and renamed the company Thorlabs Quantum Electronics, a world class developer of InP proprietary techonologies.

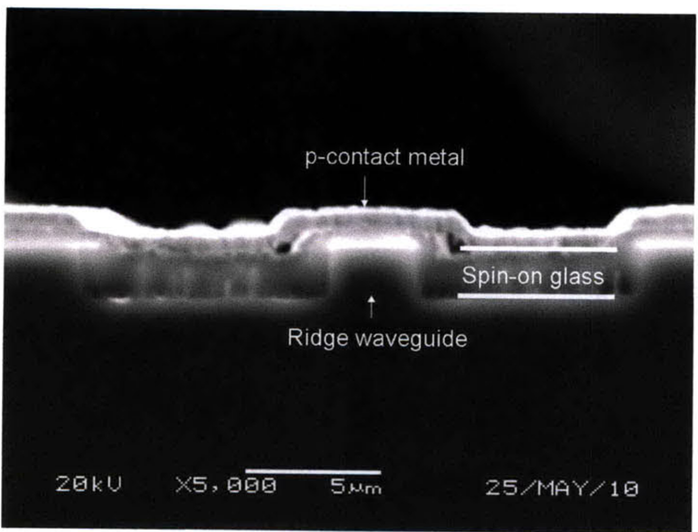

Figure 5-1: Cross-sectional SEM photograph of a ridge-stripe laser fabricated by Covega.

5.2 Laser Characterization

The processed wafer is cleaved into laser devices, with different cavity lengths, and then placed on the thermal electric (TE) cooler. After the L-I is measured for different cavity lengths, internal parameters, namely injection efficiency (η_i) and internal loss (α_i) is extracted from the behavior of inverse differential efficiency to cavity length ($1/\eta_d$-L). Changing the TE cooler temperature enables one to extract the thermal resistance of the laser diode.

VA152, VA153, VA154, and VA158 were mounted epi-side up using SnPb solder on a copper block. VA159, VA162, and VA163 were mounted in the same fashion but with epi-side down. The mounted devices were then placed on a TE cooler and electrically pumped by a pulsed or continuous laser driver. All L-I-V measurements were carried out under room temperature. A Melles Griot broadband power meter was used to detect the output power from one facet. A schematic illustration of L-I testing set up is shown in Figure 5-2. Since the power meter head only has a circular opening of 1 cm in diameter, some portion of the output power was not collected, therefore generating a coupling loss. In Figure 5-3, this loss was found to be 50% compared with Covega's measurement (see Appendix C) using an extended InGaAs detector

with integrating sphere. After correction, the power that was measured closely follows Covega's measurement when the injection level is near threshold. Power measurement only goes up to 200 mA under pulse condition, where this correcting factor is valid to apply.

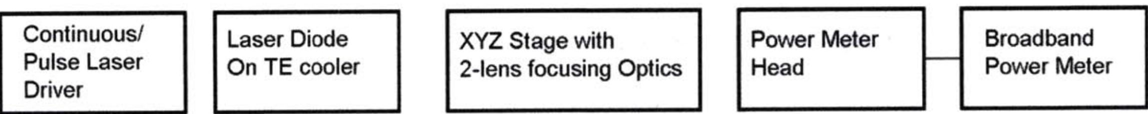

Figure 5-2: Power-current (L-I) testing set up used in the experiment.

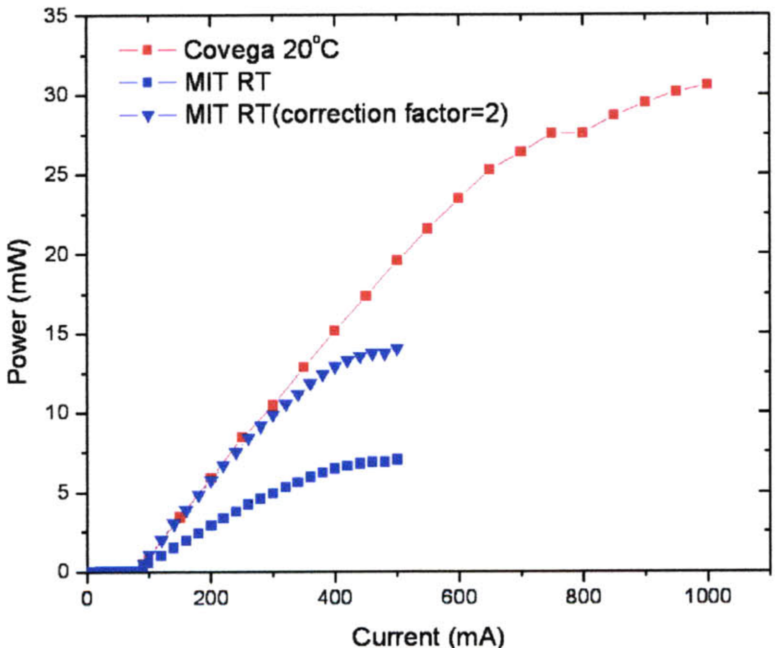

Figure 5-3: Comparison between Covega's measurement (red squares) and the measurement done in this work (blue squares). The blue triangles are the result of the multiplication of a correction factor of 2 on the measured data in this work.

5.3 Result and Discussion

5.3.1 L-I Measurement

Prior to measuring the output power from a laser diode, one should make sure the power is solely contributed from a narrow lasing bandwidth. Multiple longitudinal modes on each device is observed using the optical spectrum analyzer [see Figure 5-4(a)]. For devices mounted epi-side up, pulsed excitation with 5% duty cycle and 100ns pulse width was used to obtain L-I curve [see Figure 5-4(b)] in order to avoid threshold shift. Devices with a longer cavity show lower differential efficiency because of lower mirror loss α_m :

$$\alpha_m = \frac{1}{L}\ln(\frac{1}{R}) \tag{5.1}$$

where L is the cavity length (in cm) and R the facet reflectivity. R$\sim$0.32 for laser devices based on InP material.[1] For devices mounted epi-side down, L-I behavior under pulsed and CW conditions show good agreement; the threshold current shift is negligible under this low thermal resistant-mounting configuration. Therefore it is valid to obtain threshold and differential efficiency using CW excitation for epi-side down mounting condition.

Threshold current density J_{th} and quantum differential efficiency η_d is obtained from L-I curve. The former intersects with abscissa and the latter could be derived from the slope.

$$\eta_d = 2 \times \frac{q\lambda}{hc} \times \frac{\Delta P}{\Delta I} = \eta_i \times (\frac{\alpha_m}{\alpha_m + \langle\alpha_i\rangle}) \tag{5.2}$$

In which ΔP is the power coming out from one facet and ΔI the injection current. Since the device facets were not treated with antireflection or high reflection coatings, the factor of 2 in equation 5.2 accounts for power exiting both facets. Internal parameters of a laser is extracted from the above multiple-cavity length (L's) mea-

surement. Carrier injection efficiency η_i , and internal modal loss $\langle\alpha_i\rangle$ is obtained by curve-fitting the inverse differential efficiency. (see Figure 5-4(c), two devices with 0.1 cm and 0.15 cm cavity length was marked in hollow circle.) The relation between internal and external parameters is the following:

$$\frac{1}{\eta_d} = \frac{\alpha_i}{\eta_i \ln(\frac{1}{R})} L + \frac{1}{\eta_i} \tag{5.3}$$

Internal loss α_i is associated with optical propagation along the cavity and mainly due to the overlap of the optical mode with the high carrier density region, such as the doped cladding and the undoped quantum wells. The measured intervalence band carrier absorption on p-doped (p=10^{18} cm^{-3}) InP wafer is around 40 cm^{-1} [19], which leads to an internal loss on the order of 2 cm^{-1}; whereas the loss we obtained was one order of magnitude larger than this value. Two reasons may account for such high loss: 1) crystal defects may be present in p-cladding layers due to non-optimized epitaxial growth conditions. Figure 5-9 shows the top contact of VA154 laser structure examined with an optical microscope. Areas identified are that treated with and without chemical etch. Small elongated surface defects were observed in both regions and among all the samples grown in this thesis. 2) Unoptimized crystal quality in the active region. The broad FWHM on PL emission peak shown in Section 4.2.3 indicates structural imperfection in the active region, where multiple epi-layer interfaces reside. The photons generated within the active region may suffer from severe scattering loss.

The carrier injection efficiency η_i indicates the fraction of the terminal current that is injected into the active region as carriers. Current leakage and thermionic emission prevent carriers from entering the active region. There are several factors that may lower the injection efficiency: structure imperfection at the side wall of the ridge becomes a shunt path around the active region; the laser device is operating under high temperature or high carrier injection which enlarges the energy span of the carrier distribution and allows those high energy carriers to escape from the active region. We calculated η_i to be approximately 70%, which is comparable to most

working laser devices. Nevertheless, a better design may be a 20 μm broad area device that would ensure minimal side wall roughness. Of course, a broad area device may lead to the excitation of multiple transverse modes.

L-I-V measurements under continuous excitation are shown in Figure 5-4(d) with a diode turn-on voltage around 1V. In Figure 5-4(b), differential efficiency is lower in the device with a longer cavity whereas in Figure 5-4(d), a higher injection current (400 mA) is required to observe thermal roll off. The former is the result of the lower mirror loss in Equation 5.2 and the latter is due to better heat dissipation in the longer cavity devices. Similar trend is shown in sample VA154 (Figure 5-5), VA158 (Figure 5-6), VA159 (Figure 5-7), VA162 (Figure 5-8). For devices mounted epi-side down, the threshold current and differential efficiency measured under CW excitation are similar to those measured under pulsed excitaion. Therefore, the L-I curves shown in Figure 5-7 and Figure 5-8 were only measured under CW excitation. Note the data points used in internal parameters fitting are based on the number of working devices in the experiment. In Figure 5-10, only the lasing feature was observed in VA163. However, Covega demonstrated that VA163 is a working device. (see Appendix C)

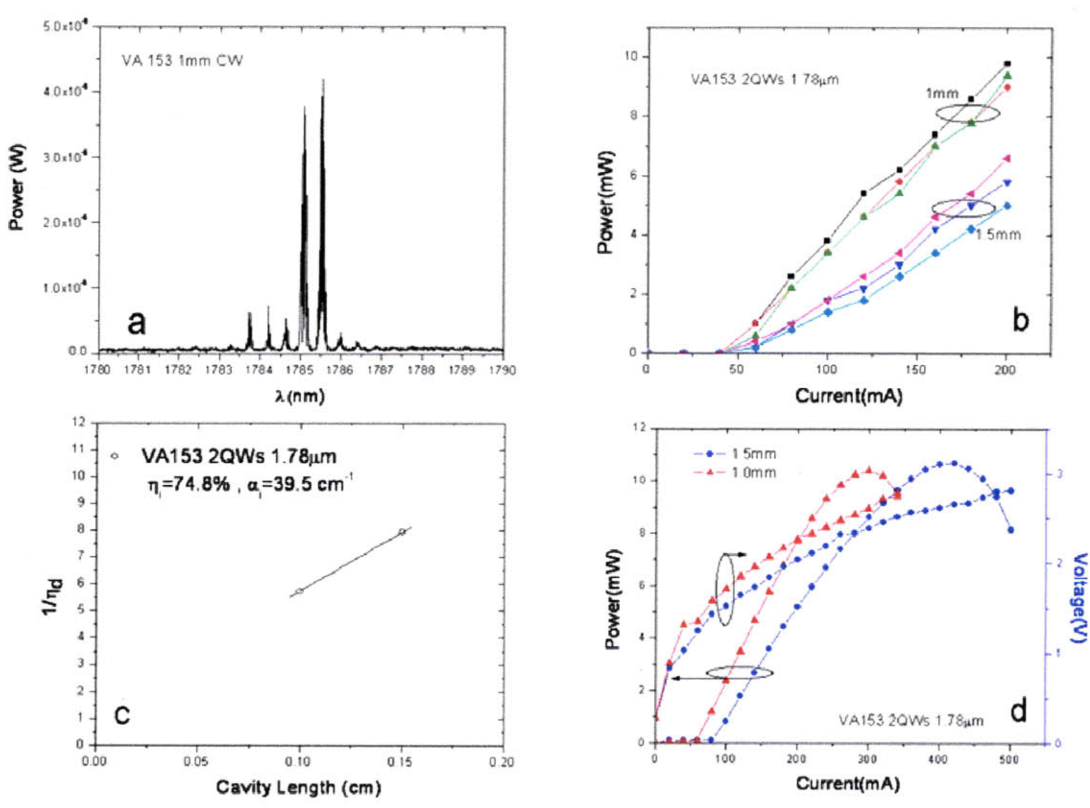

Figure 5-4: Laser VA153 (a) optical power spectrum, (b) L-I curve under pulsed excitation, (c) internal loss and injection efficiency, (d) L-I-V curve under CW excitation. All measurements are at room temperature, epi-side up.

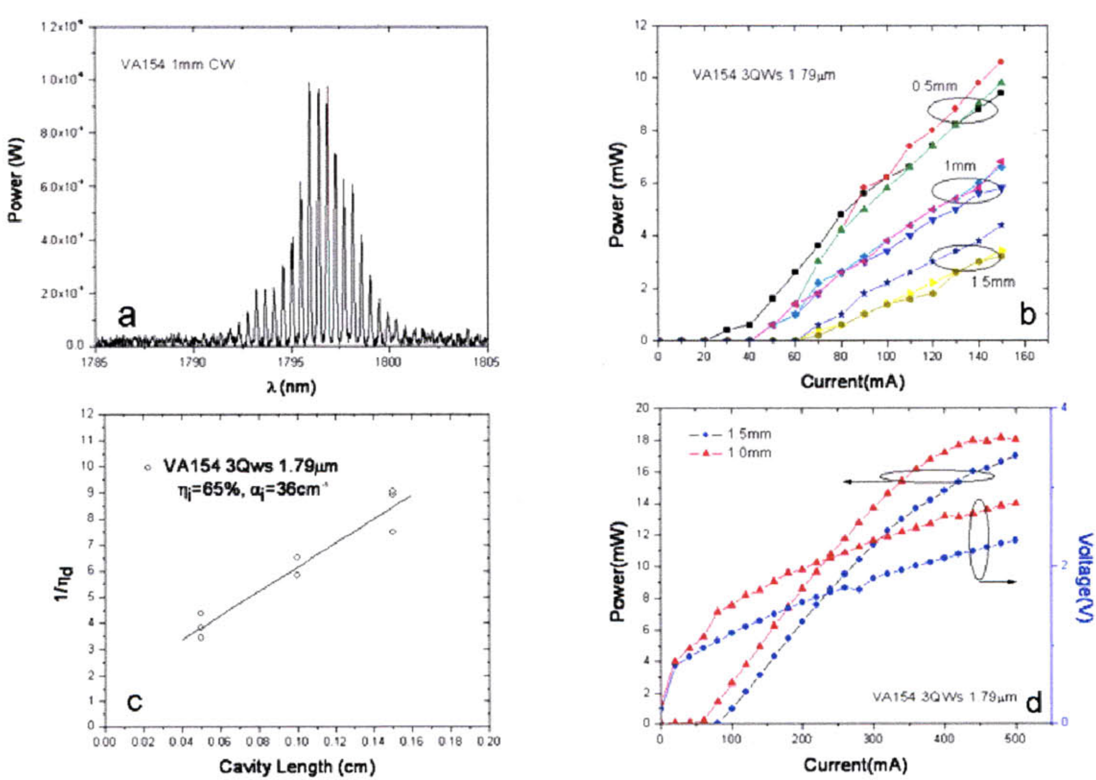

Figure 5-5: Laser VA154 (a) optical power spectrum, (b) L-I curve under pulsed excitation, (c) internal loss and injection efficiency, (d) L-I-V curve under CW excitation. All measurements are at room temperature, epi-side up.

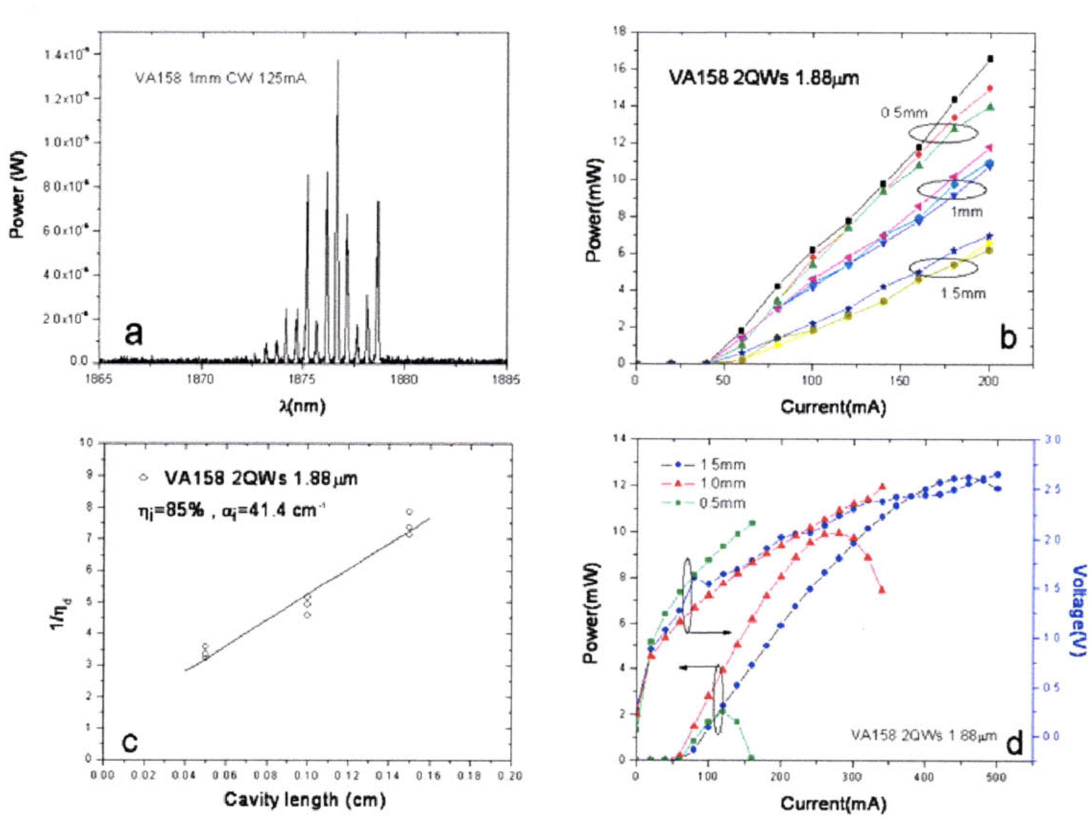

Figure 5-6: Laser VA158 (a) optical power spectrum, (b) L-I curve under pulsed excitation, (c) internal loss and injection efficiency, (d) L-I-V curve under CW excitation. All measurements are at room temperature, epi-side up.

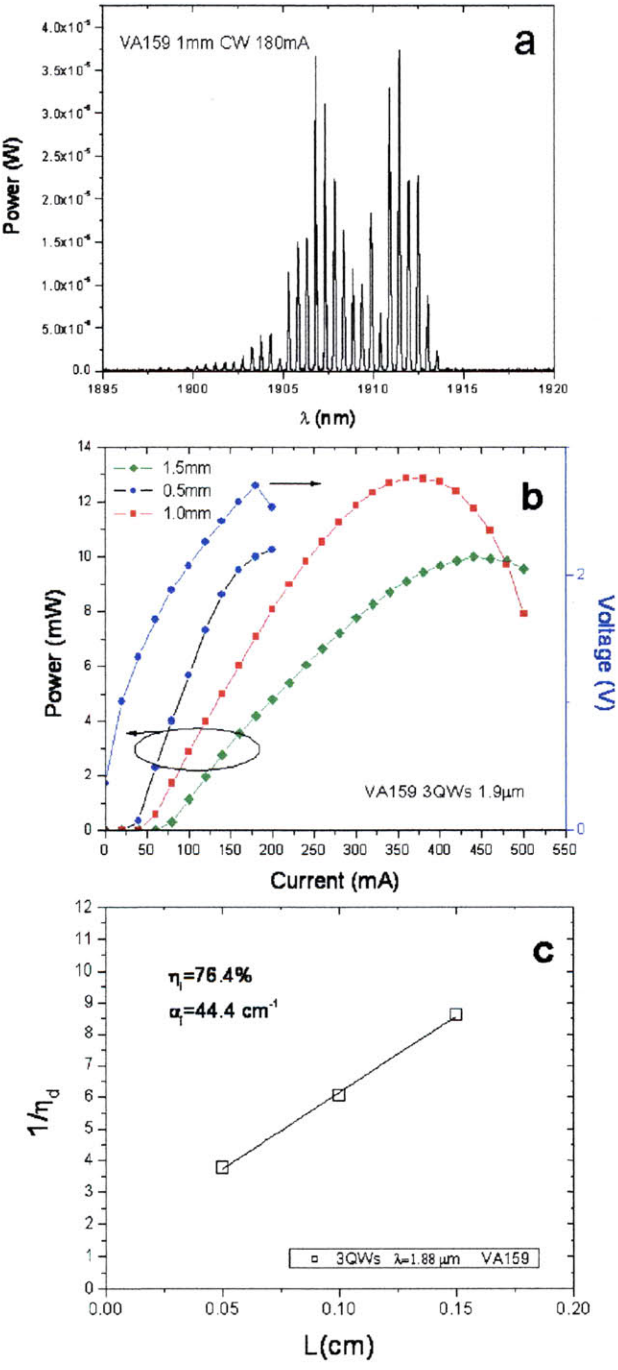

Figure 5-7: Laser VA159 (a) optical power spectrum, (b) internal loss and injection efficiency, (c) L-I-V curve under CW excitation. All measurements are at room temperature, epi-side down.

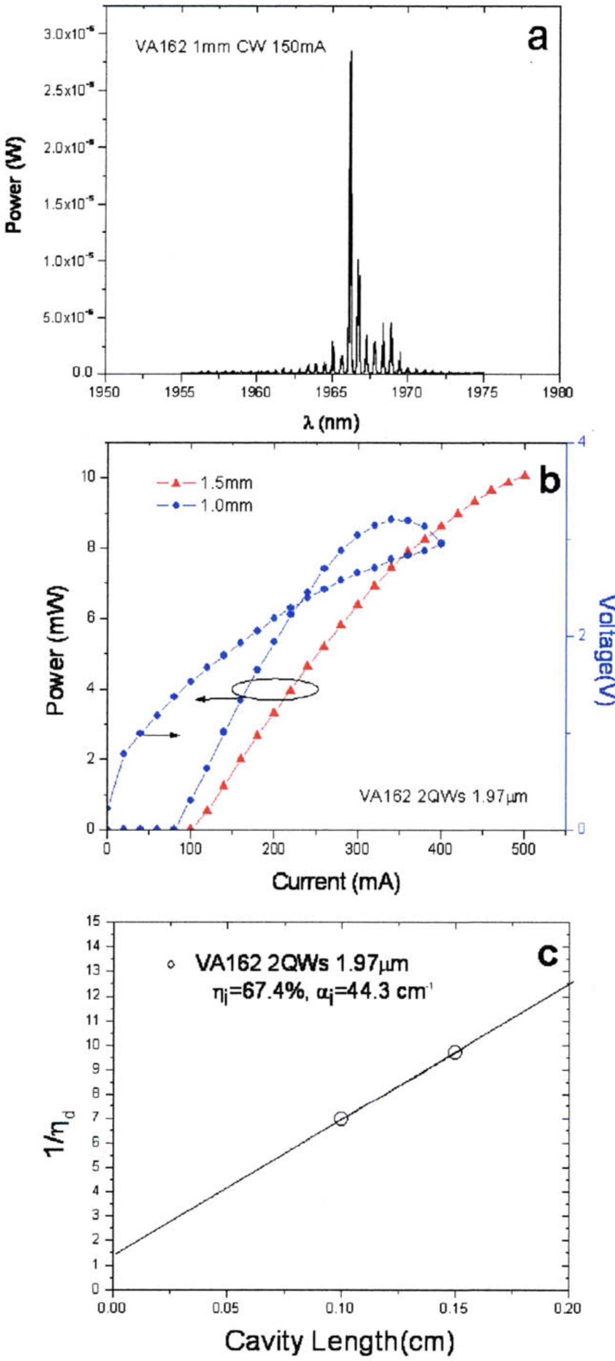

Figure 5-8: Laser VA162 (a) optical power spectrum, (b) internal loss and injection efficiency, (c) L-I-V curve under CW excitation. All measurements are at room temperature, epi-side down.

Figure 5-9: VA153 defects on the surface treated with and without the wet etch.

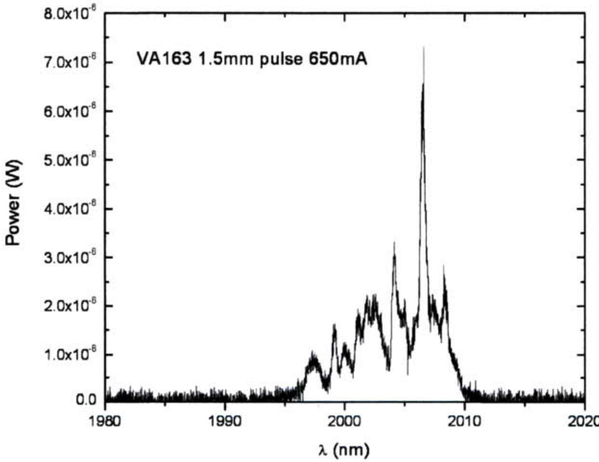

Figure 5-10: Electroluminescence spectrum of VA163 FP laser device.

5.3.2 Thermal Resistance Measurement

Thermal resistance indicates how the device temperature changes with input power. The lasing wavelength is a function of device temperature and therefore level of current injection. Knowing the change of wavelength with temperature under fixed current$\frac{\Delta\lambda}{\Delta T}|_I$, and the other way around,$\frac{\Delta\lambda}{\Delta I}|_T$, allows one to estimate the thermal resistance R_{th} in (K/W) of the device.

$$R_{th} = \frac{\Delta T}{\Delta\lambda}\frac{\Delta\lambda}{\Delta P} \tag{5.4}$$

ΔP is the thermal power, obtained by subtracting optical power output from total electrical power input. The measurement of the first term in Equation 5.4 was conducted under pulse excitation in order to minimize the heating effect contributed from current injection. The only variable in this measurement is the TE cooler temperature. The measurement of the second term in the equation was conducted under CW excitation but with a fixed TE cooler temperature. Note the constant T in the second term denotes the constant exterior temperature provided by a TE cooler as opposed to the interior temperature in the laser active region.

All devices were placed on a TE cooler for temperature adjustment. The emission wavelength was recorded from the spectrum measured by the OSA with similar testing apparatus as in the electroluminescence measurement. To adjust electrical input power, one simply changes the injection current on CW laser driver and records the voltage drop across the device. This potential difference comes from the sum of the built-in voltage and the series resistance between two terminals. Figure 5-11 shows the thermal resistance R_{th} of VA158 laser device with 1.0 mm and 1.5 mm cavity length, mounted epi-side up. High R_{th} was observed for shorter cavity devices indicating poorer heat dissipation from the active region under CW operation. In other words, under the same initial condition, providing equivalent amount of thermal power, will cause the shorter cavity device to have a higher device temperature.

Similarly, Figure 5-12 shows the same measurements on VA159 laser device mounted epi-side down. A laser device with higher R_{th} is prone to have higher threshold cur-

rent and accordingly an early thermal roll-off. However, one could leverage this phenomenon to create a sensitive tunable laser, since wavelength tuning also relies on a temperature change of the laser.

Figure 5-13 compares R_{th} under different mounting configurations. The laser devices mounted epi-side down have smaller thermal resistance because less thermal mass exists between the active region and the heat sink. Due to the insufficient data points in this figure, a fit is not able to perform based on four laser devices. The conclusion in this comparison is a clear trend stating that a lower thermal resistance could be obtained for a longer cavity device mounting epi-side down.

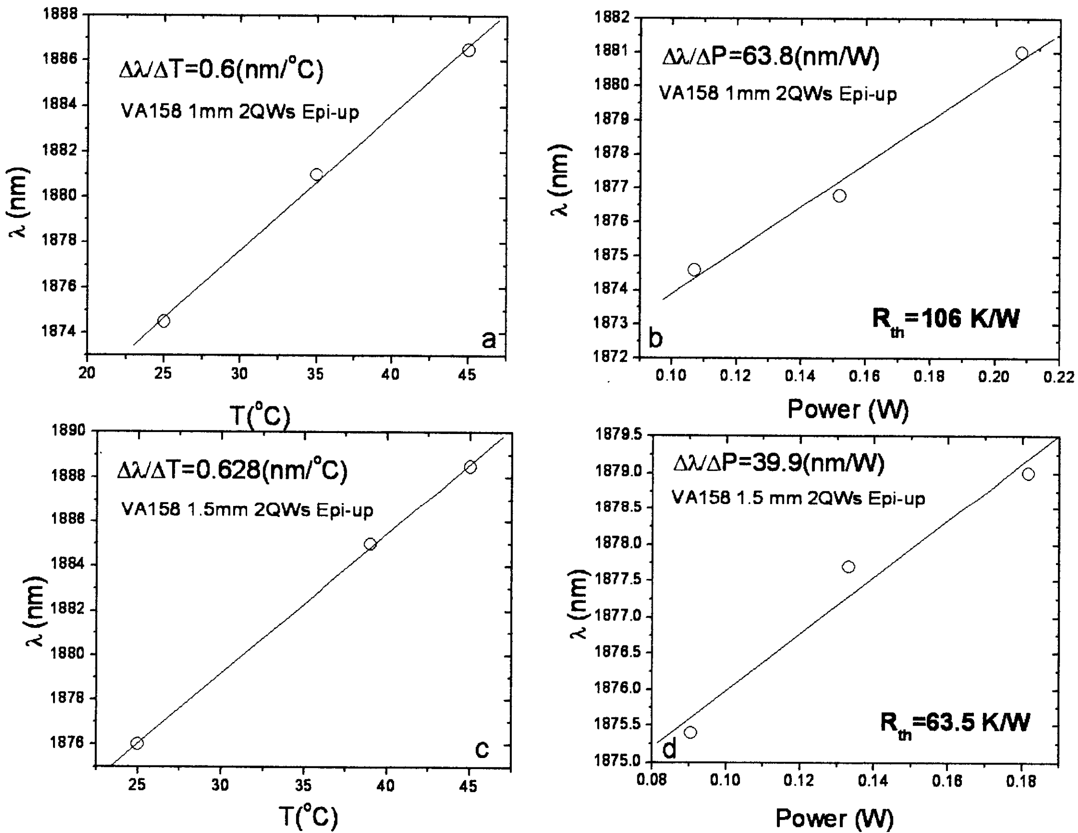

Figure 5-11: Thermal resistance measurement for the laser device VA158 mounted epi-side up: a) and b) are devices with 1.0 mm cavity; c) and d) are devices with 1.5 mm cavity.

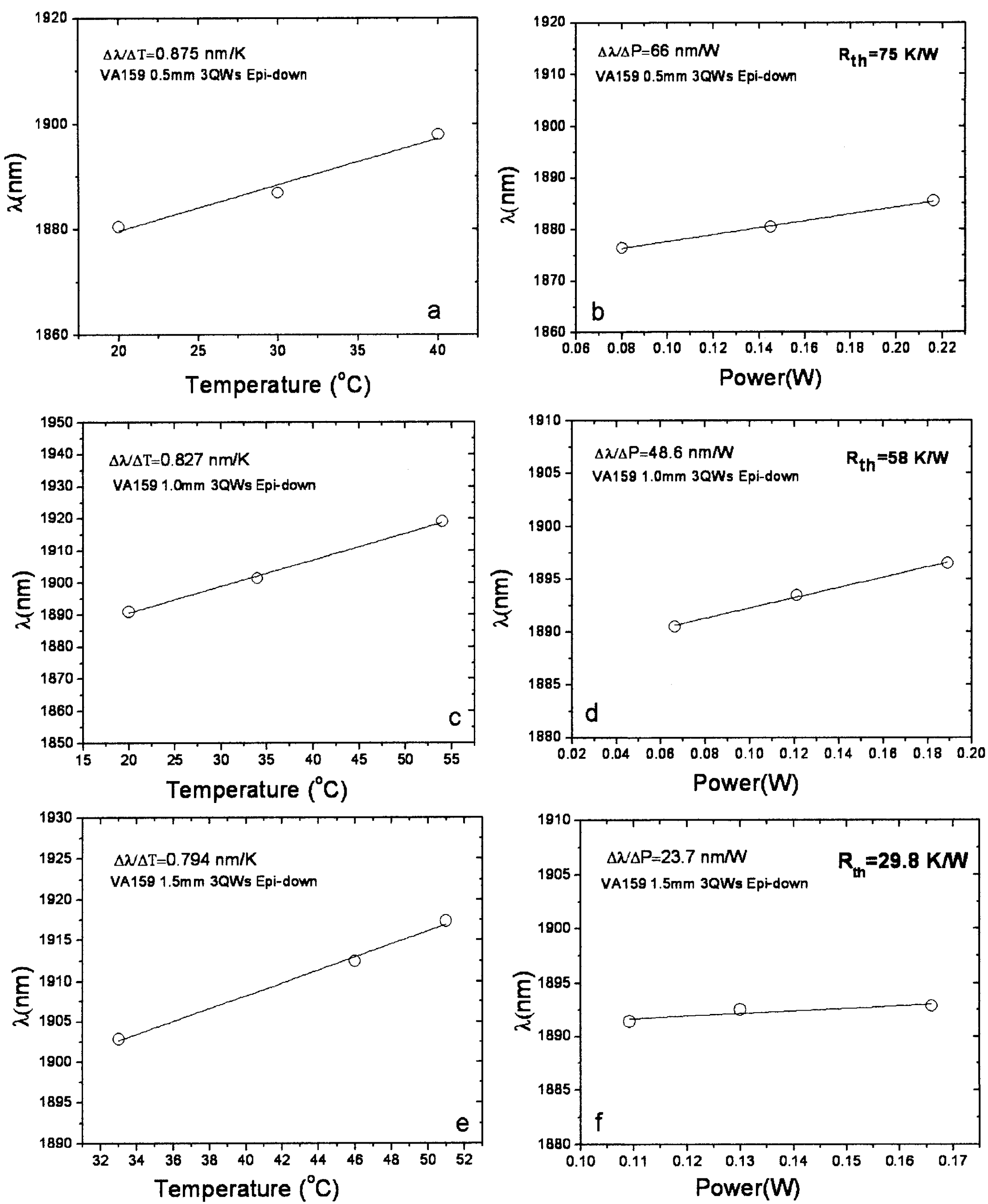

Figure 5-12: Thermal resistance measurement for the laser device VA159 mounted epi-side down: a) and b) are devices with 0.5 mm cavity; c) and d) are devices with 1.0 mm cavity; e) and f) are devices with 1.5 mm cavity.

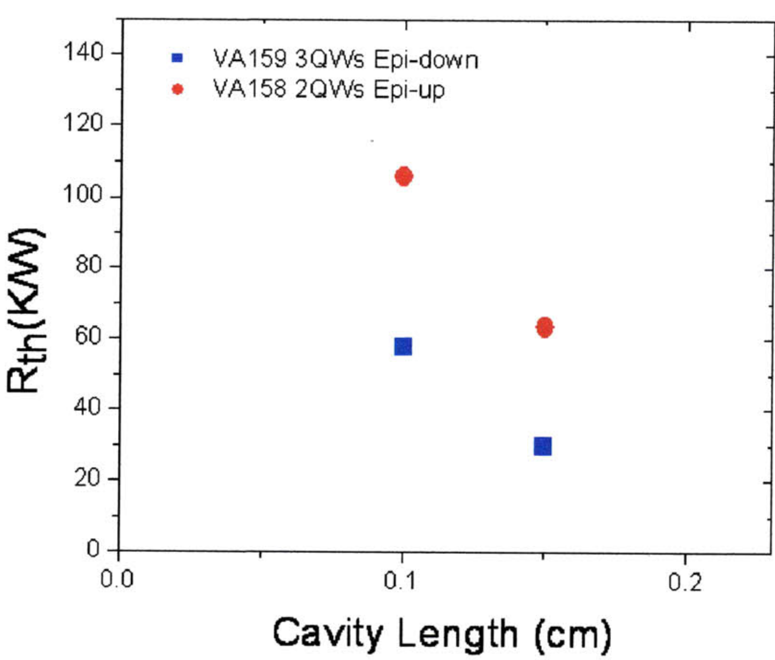

Figure 5-13: Thermal resistance with different device mounting configurations

Chapter 6

Conclusion and Future Work

This thesis presented the design, growth, fabrication, and characterization of the InGaAs strained multiple quantum well lasers on the InP substrates. The identification of the epitaxial materials, the study of the electrical, optical, and thermal property of these specific long wavelength laser devices were documented. Concluded from all the characterization results, we demonstrated 1) a 2.07 μm electroluminescence spectrum from a broad area laser device at room temperature and pulsed driving condition; and 2) a 1.97 μm wavelength emission with 10 mW output power from a ridge laser device (2 μm ridge width) at room temperature and CW driving condition. This 1.97 μm edge-emitting laser is going to be fabricated into a butterfly package with fiber pig-tail, in order to implement in the photo acoustic spectroscopy system for petrochemical trace gas detection.

6.1 Antimony-Based Material System

The mid-infrared (MIR) semiconductor laser device is of great importance in terms of ultra sensitive molecular sensing, since several crucial toxic gas molecules (CH_4, CO_2, CO, and HCl) have their fundamental absorption lines sitting in a spectrum region spanning from 2 to 3 μm. The sensing application can be achieved by MIR laser diodes operating under room temperature and outputting tens of milliwatt power in two major material systems: phosphide base and antimonide base. This thesis stud-

ied the former material system in a strained InGaAs quantum wells (QWs) structure. In this section, a brief survey of the antimonide based MIR wavelength laser structure will be presented.

An antimony-based III-V edge-emitting diode laser is commonly categorized by its band alignment. Figure 6-1 schematically shows type I, type II (staggered), and type III (broken type II) band offsets. Table 6-1 indicates laser structures within MIR (2~5 μm) range and their performance specification. Type I laser has been the work horse in 2 to 3 μm region, especially for InGaAsSb/AlGaAsSb strained quantum well laser; the laser has specific application for tunable diode laser absorption spectroscopy (TDLAS). For TDLAS, high operational temperature and low J_{th} are the main performance criteria. The advantages of type I band alignment include 1) 2-dimensional density of state in the quantum well (QW) structure, 2) improved carrier confinement, 3) convenient to tune the energy level (emission wavelength) with QW width and composition, and 4) compressive strain could couple with quantum size effect and lower hte in-plane heavy hole effecitve mass, resulting in lower J_{th}.

For longer wavelengths, type I band alignment shows decreasing characteristic temperature (T_o), output power and differential efficiency. The longest emitting wavelength reported under CW RT operation is reported to be 3.04 μm [20]. For wavelengths beyond 3 μm, no CW antimony-based diode laser operates under RT due to the large Auger coefficient, less hole confinement, and increasing expansion of the optical mode into the cladding layer. Type II "W" laser starts showing superior quality based on its low Auger recombination rate and substantial overlap between electron and hole wavefunctions. The benefit of this structure with spatial separated carriers is to tailor the longer wavelength emission by adjusting quantum confinement. The longest wavelength reported so far under CW and RT is a single stage "W" laser emitting at 4.02 μm [21].

Quantum cascade laser (QCL) is another important structure that shows extraordinary temperature stability for optical phonon scattering being the dominant non-

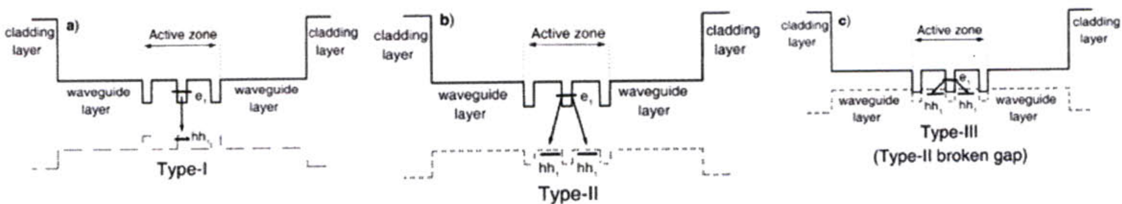

Figure 6-1: A schematic of various band alignments in the laser structures: a) Type I, b) Type II, and c) Type III (broken type II).

radiative process between intersubband transition. Interband quantum cascade laser (ICL) is analogous to a broken type II QCL. Sophisticated wavefunction engineering was exploited in these calculation- and fabrication-intense structures [22],[23].

Band Alignment	Operating condition	Band Diagram	Emission (um)	Active Structure
Type I	CW RT		3.5	AlGaAsSb / InGaAsSb
Type I	CW RT	Same above	2.4	AlGaAsSb / InGaAsSb
Type II "W"	CW T=218K		4.02	10 QW InAs/GaInSb/InAs/AlGaSb
Type II "W"	CW T=195K	Same above	3.25	10 QW InAs/GaInSb/InAs/AlGaAsSb
QCL	CW T=300K		3.3-3.8	InAs/AlSb
ICL	CW T=300K		3.3-3.8	InAs/GaInSb

Table 6.1: MIR laser diodes

6.1.1 2.3 μm Antimonide Diode Laser for Photo Acoustic Spectrometry (PAS)

Figure 6-2 illustrates the working principal and schematic of the PAS system[1]. Modulated light first passes through a plastic resonant cell containing the target gas. Non-radiative relaxation following the absorption process generates modulated heat (pressure wave), which is then detected by a built-in amplifier. In order to have a sensitive and strong signal, a high spectral purity light source is required. Therefore, a compact semiconductor laser which emits at the fundamental absorption line of the target gas is the best candidate. A widely tunable laser diode is more desirable not only for multi-gas detection but also for higher spectral sensitivity.

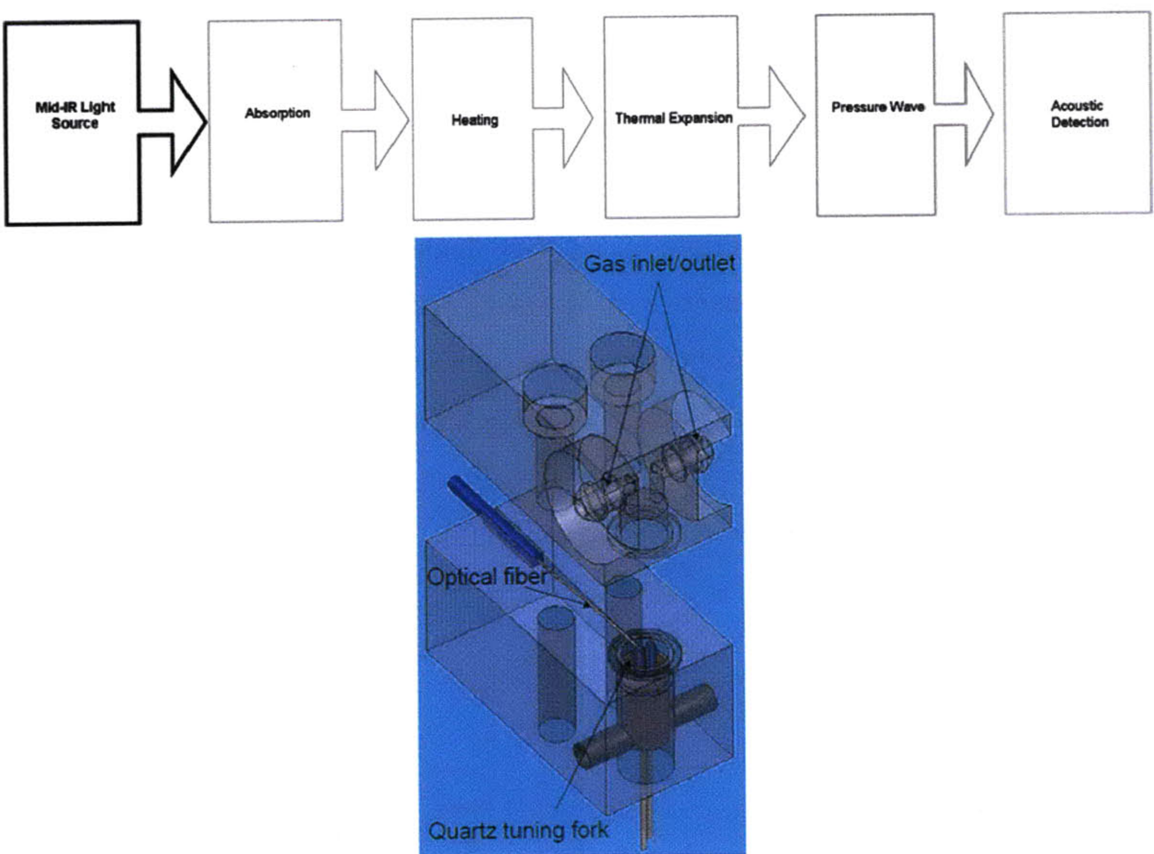

Figure 6-2: Working principal and design schematic of quartz-enhanced Photo-Acoustic Spectroscopy System.

[1]Designed by Dr. Harry Lee, MIT

6.1.2 Photonic Crystal Tunable Laser

Tunable lasers are conventionally obtained by employing a sampled grating structure. As an example, a tunable four-section cavity requires four contacts, front and rear Distributed Bragg Reflector (DBR) mirrors, and an epitaxial regrowth step. A tuning range up to 40 nm with a side-mode suppression ratio (SMSR) greater than 40 dB [24] was reported. On the other hand, a coupled-cavity tunable laser [24] was also reported but suffers due to a complex fabrication process. By combining the 2-D gratings and coupled-cavity design, the photonic crystals (PhCs) tunable laser achieves single mode tuning over a comparable range as in DBR laser. Currently 47 nm of tuning range and 40 dB SMSR was reported [25]. In antimonide material system, aluminum is usually used in the thick cladding layer, which limits the regrow crystal quality. 2-D PhCs coupled cavity laser avoids unrealistic DBR fabrication in Al-containing antimonide system and bring along several advantages [26]: 1) easy control of cavity length and mirror reflectivity, 2) very simple technological process [27], 3) small component footprints which allow higher chip integration density, 4) easy to integrate other components such as wavelength monitors [28], and 5) unlike the sample gratings, the PhCs cavity displays an almost flat spectral response, leading to potentially very large tuning range. The only limitation is the gain curve of the active medium.

6.2 Extension to Longer Wavelength-Dilute Nitrogen Mateirals

From Section 6.1, type II "W" and QCL lasers are good candidates to extend the wavelength to 3~5 μm range. InAs/GaInSb and InAs/AlSb superlattice is the material considered to match special band alignment, which in practice is challenging in MBE growth, since the four layers of the "W" structure contain three distinct materials with growth temperatures that differ by more than 100°C. The interface chemistry is complex since the adjacent layers share neither a common cation nor a common anion. Interfacial bond type (GaAs- or InSb-like) is also sensitive to laser performance. Not only are these structures are challenging to grow, but the performance is also unsatisfactory in terms of RT operation. An alternative to (AlGaIn)-(PAsSb) material system starts to emerge by introducing dilute nitrogen ($\leq 5\%$) into the epitaxial active region.

GaInNAs material system is of interest to realize low-cost telecommunication (1.3~1.55 μm) lasers [29]. To reach MIR wavelength region, smaller bandgap InAsN active material has been fabricated [30] and proposed [31],[32] on InP and InAs substrates. Dilute nitride antimonide alloy with even narrower band gap has received less attention both theoretically and experimentally. Band anticrossing model (BAC) is now well established for explaining conduction band splitting in dilute nitride materials. BAC is essentially the interaction between spatially-localized nitrogen states and the conduction band of the underlying nitrogen-free semiconductor. This model yields the following dispersion relations for the two coupled bands:

$$E_{\pm}(k) = \frac{1}{2} \times \left\{ [E_C(k) + E_N] \pm \sqrt{[E_C(k) - E_N]^2 + 4V^2 x} \right\} \qquad (6.1)$$

where $E_C(k)$ is the conduction band dispersion of the unperturbed (nitrogen free) semiconductor, E_N the isoelectronic level of the nitrogen, $E_{\pm}$ the split (perturbed) conduction bands; V is the interaction potential between $E_C(k)$ and E_N; x is the nitrogen fraction.

A recent theoretical study combines type II band alignment with dilute nitride material [33]. An InAsN/GaSb/InAsN "W" quantum well lattice-matched to InAs substrate was designed to operate at 3.3 μm, RT. The calculation was performed by using 10-band k $\bullet$ p Hamiltonian including strain and BAC. First, layer thickness and quantum well numbers were determined from optical momentum matrix element optimization. This involes the calculation of energy levels and wave function overlap. Second, $E - k$ dispersion and carrier distribution derive gain spectrum and Auger coefficient under various temperature. By evaluating a reasonable optical loss in this design, a threshold current density is estimated to be 500 A/cm^2, implying dilute-nitride InAsN/GaSb/InAsN "W" quantum wells are suitable for mid-infrared laser operation at RT. In reality, nitrogen incorporation in the epitaxial film remains a challenging topic. The difficulties include the limited solubility of nitrogen atoms, phase segregation, nonradiative defects caused by the low growth temperature, and ion damage from the nitrogen plasma source.[34] Based on the abundant theoretical study on this promising new material system, the unsolved problem in material realization is surely a very interesting topic for material scientists.

Appendix A

Sample ID

The first part of each sample ID is the purpose and proposed structure for this epitaxy run. QW composition, expected PL emission wavelength, QW numbers, and real substrate temperature (DRS measurement) were denoted on the title. Layer by layer composition, growth time, intended thickness, doping level, and lattice mismatch were detailed in the table. The second part of each sample ID includes MBE flux condition, HRXRD (004) $2\theta/\omega$ spectrum, and PL spectrum. Group III beam equivalent pressure (BEP), group V base temperature (°C) and valve position (mil) were documented in the lower left table. The third part of the sample ID records the final structure data obtained by fitting the HRXRD spectrum in LEPTOS program.

VA153 In(0.65)Ga(0.35)As Laser 1750nm 2QWs 508C

To grow a 1.75um laser with 2 In0.65GaAs QWs
Corresponding PL structure is VA151; Corresponding Laser Structures are VA150 and VA152
2 wafers grown; one is to be shipped to Covega for Processing

In1(0.53)Ga1As:Be	5.14min	100nm	3e19 LM
In12P:Be	23.57min	500nm	1e18 =>1e19
In12P:Be	70.71min	1500nm	1e18
In2(0.53)Ga2(0.313)Al(0.156)As:Be	0.985min	20nm	1e18 LM
In1P:Be	7.071min	150nm	3e17
In2(0.53)Ga2(0.313)Al(0.156)As	8.862min	180nm	LM
In2(0.53)Ga2(0.313)Al(0.156)As	0.985min	20nm	LM
In12(0.65)Ga1As	0.265min	8nm	0.8%CS
In2(0.53)Ga2(0.313)Al(0.156)As	0.985min	20nm	LM
In12(0.65)Ga1As	0.265min	8nm	0.8%CS
In2(0.53)Ga2(0.313)Al(0.156)As:Si	9.847min	200nm	LM
In1P :Si	23.57min	500nm	3e17
In1P buffer:Si	23.57min	500nm	1e18
InP (S-doped)			

VA153 In(0.65)Ga(0.35)As Laser 1750nm 2QWs 508C

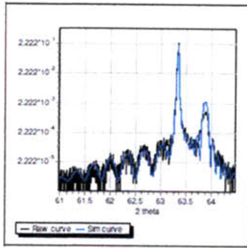

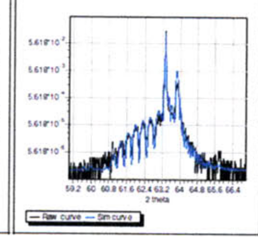

BEP_In1	5.65E-07 Torr
BEP_In2	2.72E-07 Torr
BEP_Ga1	4.46E-07 Torr
BEP_Ga2	2.22E-07 Torr
BEP_Al	0.35E-07 Torr
BEP_As/Valve_As	114E-07/280
BEP_P/Valve_P	133E-07/297
T_sub/DRS	600C/508C

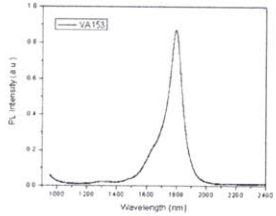

VA153 In(0.65)Ga(0.35)As Laser 1750nm 2QWs 508C

In1(0.527)Ga1As(0.89)P:Be	5.14min	99.6nm	3e19 0.39%TS
In12As(0.0014)P:Be	23.57min	496.5nm	1e18 =>1e19
In12As(0.0001)P:Be	70.71min	1506nm	1e18
In2Ga2(0.355)Al(0.145)As:Be	0.985min	17.7nm	1e18 0.2%TS
In1As(0.0084)P:Be	7.071min	155nm	3e17
In2Ga2(0.33Al(0.14)As	8.862min	201.8nm	0.007%CS
In2Ga2(0.33)Al(0.135)As	0.985min	23.7nm	0.007%CS
In12(0.665)Ga1As	0.265min	6.78nm	0.9%CS
In2Ga2(0.33)Al(0.14)As	0.985min	23.7nm	0.007%CS
In12(0.665)Ga1As	0.265min	6.78nm	0.9%CS
In2Ga2(0.33)Al(0.14)As:Si	9.847min	217nm	0.007%CS
In1As(0.0065)P :Si	23.57min	515nm	3e17
In1As(0.001)P buffer:Si	23.57min	473nm	1e18
InP (S-doped)			

VA154 In(0.65)Ga(0.35)As Laser 1750nm 3QWs 485C

To grow a 1.75um laser with 3 In0.65GaAs QWs
Corresponding PL structure is VA151; Corresponding Laser Structures are VA153 and 1.55 um versions: VA150 and VA152
2 wafers grown; one is to be shipped to Covega for Processing

In1(0.53)Ga1As:Be	5.159min	100nm	3e19	LM
In12P:Be	23.51min	500nm	1e18 =>1e19	
In12P:Be	70.525min	1500nm	1e18	
In2(0.53)Ga2(0.313)Al(0.156)As:Be	0.98min	20nm	1e18	LM
In1P:Be	7.052min	150nm	3e17	
In2(0.53)Ga2(0.313)Al(0.156)As	8.819min	180nm		LM
In2(0.53)Ga2(0.313)Al(0.156)As	0.98min	20nm		LM
In12(0.65)Ga1As	0.265min	8nm		0.8%CS
In2(0.53)Ga2(0.313)Al(0.156)As	0.98min	20nm		LM
In12(0.65)Ga1As	0.265min	8nm		0.8%CS
In2(0.53)Ga2(0.313)Al(0.156)As	0.98min	20nm		LM
In12(0.65)Ga1As	0.265min	8nm		0.8%CS
In2(0.53)Ga2(0.313)Al(0.156)As:Si	9.799min	200nm		LM
In1P :Si	23.51min	500nm	3e17	
In1P buffer:Si	23.51min	500nm	1e18	
InP (S-doped)				

VA154 In(0.65)Ga(0.35)As Laser 1750nm 3QWs 485C

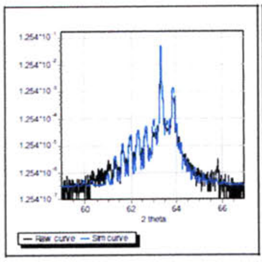

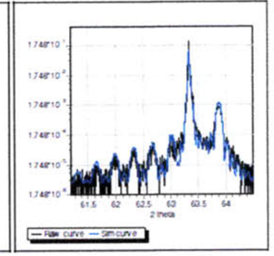

BEP_In1	5.64E-07 Torr
BEP_In2	2.73E-07 Torr
BEP_Ga1	4.42E-07 Torr
BEP_Ga2	2.22E-07 Torr
BEP_Al	0.353E-07 Torr
BEP_As/Valve_As	114E-07/280
BEP_P/Valve_P	122E-07/297
T_sub/DRS	590C/485C

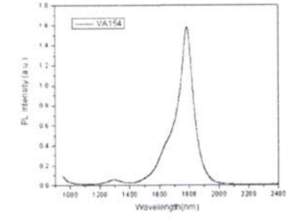

VA154 In(0.65)Ga(0.35)As Laser 1750nm 3QWs 485C

In1(0.53)Ga1As(0.89)P:Be	5.159min	106.7nm	3e19	0.37%TS
In12As(0.0047)P:Be	23.51min	498.5nm	1e18 =>1e19	
In12As(0.0015)P:Be	70.525min	1516.8nm	1e18	
In2Ga2(0.368)Al(0.15)As:Be	0.98min	17.21nm	1e18	0.32%TS
In1As(0.0115)P:Be	7.052min	164.4nm	3e17	
In2Ga2(0.335)Al(0.14)As	8.819min	195nm		0.027%TS
In2Ga2(0.32)Al(0.145)As	0.98min	23nm		0.04%CS
In12(0.66)Ga1As	0.265min	7.25nm		0.88%CS
In2Ga2(0.32)Al(0.145)As	0.98min	23nm		0.04%CS
In12(0.66)Ga1As	0.265min	7.25nm		0.88%CS
In2Ga2(0.32)Al(0.145)As	0.98min	23nm		0.04%CS
In12(0.66)Ga1As	0.265min	7.25nm		0.88%CS
In2Ga2(0.33)Al(0.14)As:Si	9.799min	190nm		0.04%CS
In1As(0.0003)P :Si	23.51min	504nm	3e17	
In1P buffer:Si	23.51min	483nm	1e18	
InP (S-doped)				

VA156 In(0.7)GaAs PL 1900nm 2QWs 493C

To grow a 1.9um PL Structure with 2 Strained In0.7GaAs QWs
The two In0.7GaAs quantum wells are clad with InGaAlAs
The entire structure will be grown at a slightly higher temperature than usual (same temp at VA150)

In12P	5.722min	60nm	
In2(0.53)Ga2(0.315)Al(0.155)As	3.033min	60nm	LM
In12(0.7)Ga1(0.3)As	0.353min	8nm	1.16%CS
In2(0.53)Ga2(0.315)Al(0.155)As	1.011min	20nm	LM
In12(0.7)Ga1(0.3)As	0.353min	8nm	1.16%CS
In2(0.53)Ga2(0.315)Al(0.155)As	3.033min	60nm	LM
In2P buffer	27.22min	180nm	
InP			

BEP_In1	3.57E-07 Torr
BEP_In2	2.65E-07 Torr
BEP_Ga1	2.75E-07 Torr
BEP_Ga2	2.15E-07 Torr
BEP_Al	0.344E-07 Torr
BEP_As/Valve_As	114E-07/270
BEP_P/Valve_P	118E-07/297
T_sub/DRS	600C/493C

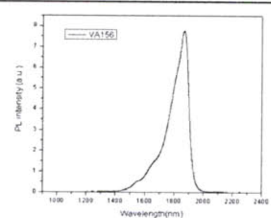

VA156 In(0.7)GaAs PL 1900nm 2QWs 493C

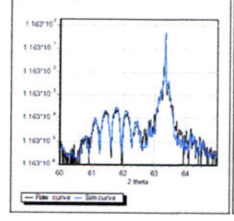

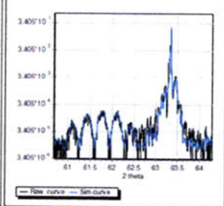

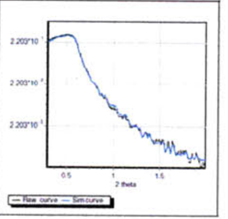

In12(As0.0012)P	5.722min	63.2nm	
In2(0.523)Ga2(0.334)Al(0.143)As	3.033min	62.9nm	0.04%TS
In12(0.713)Ga1(0.287)As	0.353min	9.26nm	1.253%CS
In2(0.523)Ga2(0.334)Al(0.143)As	1.011min	20.64nm	0.04%TS
In12(0.713)Ga1(0.287)As	0.353min	9.26nm	1.253%CS
In2(0.523)Ga2(0.334)Al(0.143)As	3.033min	63.42nm	0.04%TS
In2P buffer	27.22min	215.9nm	
InP			

VA158 In(0.75)GaAs Laser 2QWs 487C

To grow a 1.85um laser with 2 In0.75GaAs QWs
Corresponding PL structure is VA156; Corresponding Laser Structures are VA150 and VA152 (1.55um) and VA153 and VA154 (1.75um)
2 wafers grown; one is to be shipped to Covega for Processing

In1(0.53)Ga1As:Be	8.219min	100nm	3e19	LM
In12P:Be	29.495min	500nm	1e18 =>1e19	
In12P:Be	88.48min	1500nm	1e18	
In2(0.53)Ga2(0.313)Al(0.156)As:Be	1.027min	20nm	1e18	LM
In1P:Be	8.848min	150nm	3e17	
In2(0.53)Ga2(0.313)Al(0.156)As	9.244min	180nm		LM
In2(0.53)Ga2(0.313)Al(0.156)As	1.027min	20nm		LM
In12(0.75)Ga1As	0.356min	8nm		1.5%CS
In2(0.53)Ga2(0.313)Al(0.156)As	1.027min	20nm		LM
In12(0.75)Ga1As	0.356min	8nm		1.5%CS
In2(0.53)Ga2(0.313)Al(0.156)As:Si	10.275min	200nm		LM
In1P :Si	29.495min	500nm	3e17	
In1P buffer:Si	29.495min	500nm	1e18	
InP (S-doped)				

VA158 In(0.75)GaAs Laser 2QWs 487C

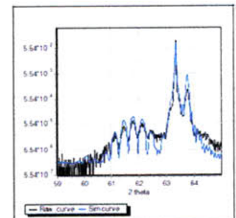

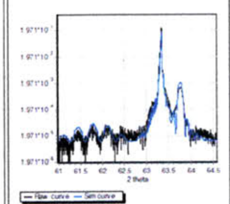

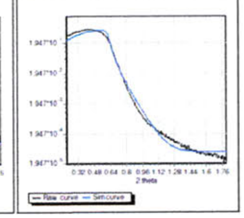

BEP_In1	3.58E-07 Torr
BEP_In2	2.6E-07 Torr
BEP_Ga1	2.74E-07 Torr
BEP_Ga2	2.13E-07 Torr
BEP_Al	0.332E-07 Torr
BEP_As/Valve_As	112E-07/270
BEP_P/Valve_P	119E-07/297
T_sub/DRS	590C/487C

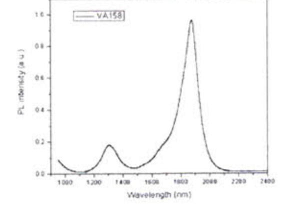

VA158 In(0.75)GaAs Laser 2QWs 487C

In1(0.5425)Ga1AsP(0.11):Be	8.219min	98.15nm	3e19	0.3%TS
In12(As0.000004)P:Be	29.495min	491nm	1e18 =>1e19	
In12(As0.000005)P:Be	88.48min	1461nm	1e18	
In2(0.548)Ga2(0.328)Al(0.124)As:Be	1.027min	25nm	1e18	0.13%CS
In1P:Be	8.848min	136nm	3e17	
In2(0.527)Ga2(0.33)Al(0.143)As	9.244min	199nm		0.01%TS
In2(0.525)Ga2(0.35)Al(0.125)As	1.027min	20nm		0.03%TS
In12(0.71)Ga1As	0.356min	9.65nm		1.23%CS
In2(0.525)Ga2(0.35)Al(0.125)As	1.027min	20nm		0.03%TS
In12(0.71)Ga1As	0.356min	9.65nm		1.23%CS
In2(0.526)Ga2(0.33)Al(0.144)As:Si	10.275min	250nm		0.02%CS
In1P :Si	29.495min	468nm	3e17	
In1(As0.00564)P buffer:Si	29.495min	459nm	1e18	
InP (S-doped)				

VA159 In(0.7)GaAs Laser 3QWs 489C

To grow a 1.85um laser with 3 In0.70GaAs QWs
Corresponding PL structure is VA156; Corresponding Laser Structures are VA158 (1.85um), VA150 and VA152 (1.55um), and VA153 and VA154 (1.75um)
2 wafers grown; one is to be shipped to Covega for Processing

In1(0.53)Ga1As:Be	8.234min	100nm	3e19	LM
In12P:Be	29.02min	500nm	1e18 =>1e19	
In12P:Be	87.05min	1500nm	1e18	
In2(0.53)Ga2(0.313)Al(0.156)As:Be	1.016min	20nm	1e18	LM
In1P:Be	8.705min	150nm	3e17	
In2(0.53)Ga2(0.313)Al(0.156)As	9.146min	180nm		LM
In2(0.53)Ga2(0.313)Al(0.156)As	1.016min	20nm		LM
In12(0.7)Ga1As	0.352min	8nm		1.16%CS
In2(0.53)Ga2(0.313)Al(0.156)As	1.016min	20nm		LM
In12(0.7)Ga1As	0.352min	8nm		1.16%CS
In2(0.53)Ga2(0.313)Al(0.156)As	1.016min	20nm		LM
In12(0.7)Ga1As	0.352min	8nm		1.16%CS
In2(0.53)Ga2(0.313)Al(0.156)As:Si	10.162min	200nm		LM
In1P :Si	29.02min	500nm	3e17	
In1P buffer:Si	29.02min	500nm	1e18	
InP (S-doped)				

VA159 In(0.7)GaAs Laser 3QWs 489C

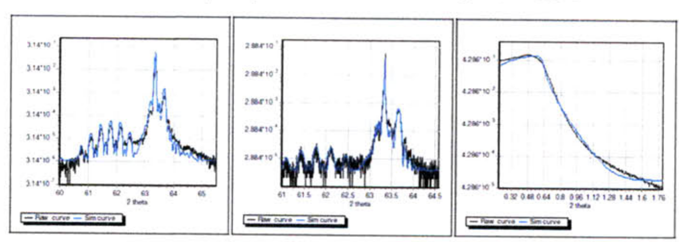

BEP_In1	3.61E-07 Torr
BEP_In2	2.66E-07 Torr
BEP_Ga1	2.7E-07 Torr
BEP_Ga2	2.13E-07 Torr
BEP_Al	0.331E-07 Torr
BEP_As/Valve_As	114E-07/270
BEP_P/Valve_P	119E-07/297
T_sub/DRS	590C/489C

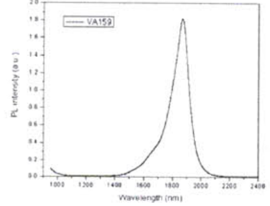

VA159 In(0.7)GaAs Laser 3QWs 489C

In1(0.55)Ga1P(0.11)As:Be	8.234min	98nm	3e19	0.24%TS
In12(As0.000001)P:Be	29.02min	511nm	1e18 =>1e19	
In12(As0.00544)P:Be	87.05min	1510nm	1e18	
In2(0.557)Ga2(0.306)Al(0.137)As:Be	1.016min	22.37nm	1e18	0.19%CS
In1As(0.000034)P:Be	8.705min	157.8nm	3e17	
In2(0.53)Ga2(0.32)Al(0.15)As	9.146min	185nm		0.008%CS
In2(0.53)Ga2(0.32)Al(0.15)As	1.016min	21nm		0.008%CS
In12(0.71)Ga1As	0.352min	8.69nm		1.23%CS
In2(0.53)Ga2(0.32)Al(0.15)As	1.016min	21nm		0.008%CS
In12(0.71)Ga1As	0.352min	8.69nm		1.23%CS
In2(0.53)Ga2(0.32)Al(0.15)As	1.016min	21nm		0.008%CS
In12(0.71)Ga1As	0.352min	8.69nm		1.16%CS
In2(0.53)Ga2(0.32)Al(0.15)As:Si	10.162min	186nm		0.008%CS
In1(As0.003)P :Si	29.02min	503nm	3e17	
In1(As0.000012)P buffer:Si	29.02min	412nm	1e18	
InP (S-doped)				

VA161 In(0.77)GaAs PL 2QWs 489C

To grow a 1.95um PL Structure with 2 Strained In0.77GaAs QWs
The two In0.77GaAs quantum wells are clad with InGaAlAs
The entire structure will be grown at a slightly higher temperature than usual (same temp at VA150)

In1P	13.03min	60nm	
In2(0.53)Ga2(0.315)Al(0.1551)As	3.18min	60nm	0.018%CS
In1(0.77)Ga1(0.23)As	0.438min	8nm	1.646%CS
In2(0.53)Ga2(0.315)Al(0.1551)As	1.06min	20nm	0.018%CS
In1(0.77)Ga1(0.23)As	0.438min	8nm	1.646%CS
In2(0.53)Ga2(0.315)Al(0.1551)As	3.18min	60nm	0.018%CS
In2P buffer	18.02min	180nm	
InP			

BEP_In1	2.49E-07 Torr
BEP_In2	2.52E-07 Torr
BEP_Ga1	1.82E-07 Torr
BEP_Ga2	2.04E-07 Torr
BEP_Al	0.33E-07 Torr
BEP_As/Valve_As	114E-07/280
BEP_P/Valve_P	119E-07/297
T_sub/DRS	600C/489C

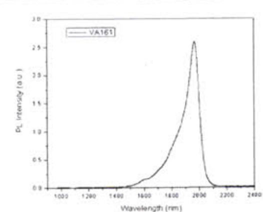

VA161 In(0.77)GaAs PL 2QWs 489C

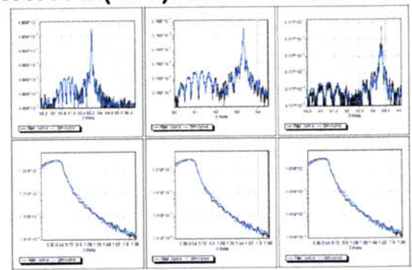

In1As(0.0189)P	13.03min	52.1nm	0.06%CS
In2(0.52)Ga2(0.323)Al(0.157)As	3.18min	47nm	0.006%TS
In2(0.528)Ga2(0.312)Al(0.16)As	3.18min	21.6nm	0.004%TS
In1(0.764)Ga1(0.236)As	0.438min	8.939nm	1.6%CS
In2(0.528)Ga2(0.312)Al(0.16)As	1.06min	21.6nm	0.004%TS
In1(0.764)Ga1(0.236)As	0.438min	8.939nm	1.6%CS
In2(0.526)Ga2(0.345)Al(0.129)As	3.18min	64.5nm	0.02%TS
In2As(0.0127)P buffer	18.02min	182nm	
InP			

VA162 In(0.76)GaAs Laser 2QWs 489C

To grow a 1.95um laser with 2 In0.76GaAs QWs
Corresponding PL structure is VA161; Corresponding Laser Structures are VA150 and VA152 (1.55um), VA153 and VA154 (1.75um) and VA158 and VA159 (1.85um)
2 wafers grown; one is to be shipped to Covega for Processing

Layer	Time	Thickness	Doping	Strain
In1(0.53)Ga1As:Be	12.217min	100nm	3e19	LM
In12P:Be	34.32min	500nm	1e18 =>1e19	
In12P:Be	102.96min	1500nm	1e18	
In2(0.53)Ga2(0.313)Al(0.156)As:Be	1.061min	20nm	1e18	LM
In1P:Be	10.296min	150nm	3e17	
In2(0.53)Ga2(0.313)Al(0.156)As	9.546min	180nm		LM
In2(0.53)Ga2(0.313)Al(0.156)As	1.061min	20nm		LM
In12(0.76)Ga1As	0.441min	8nm		1.57%CS
In2(0.53)Ga2(0.313)Al(0.156)As	1.061min	20nm		LM
In12(0.76)Ga1As	0.441min	8nm		1.57%CS
In2(0.53)Ga2(0.313)Al(0.156)As:Si	10.61min	200nm		LM
In1P :Si	32.32min	500nm	3e17	
In1P buffer:Si	34.32min	500nm	1e18	
InP (S-doped)				

VA162 In(0.76)GaAs Laser 2QWs 489C

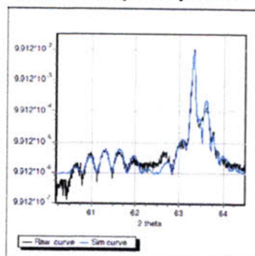

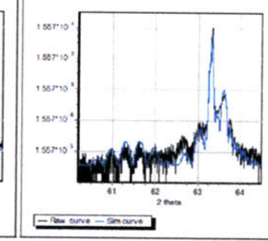

Parameter	Value
BEP_In1	2.49E-07 Torr
BEP_In2	2.51E-07 Torr
BEP_Ga1	1.77E-07 Torr
BEP_Ga2	2.04E-07 Torr
BEP_Al	0.33E-07 Torr
BEP_As/Valve_As	114E-07/280
BEP_P/Valve_P	118E-07/297
T_sub/DRS	600C/489C

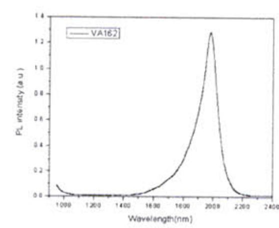

VA162 In(0.76)GaAs Laser 2QWs 489C

Layer	Time	Thickness	Doping	Strain
In1(0.55)Ga1As(0.9)P:Be	12.217min	101nm	3e19	0.2%TS
In12P:Be	34.32min	503.7nm	1e18 =>1e19	
In12As(0.001)P:Be	102.96min	1574.6nm	1e18	
In2(0.49)Ga2(0.344)Al(0.176)As:Be	1.061min	15.97nm	1e18	0.698%CS
In1As(0.0155)P:Be	10.296min	171.28nm	3e17	
In2(0.53)Ga2(0.32)Al(0.15)As	9.546min	171.36nm		0.008%CS
In2(0.534)Ga2(0.317)Al(0.149)As	1.061min	20.73nm		0.035%CS
In12(0.739)Ga1As	0.441min	9.24nm		1.43%CS
In2(0.534)Ga2(0.317)Al(0.149)As	1.061min	20.73nm		0.035%CS
In12(0.739)Ga1As	0.441min	9.24nm		1.43%CS
In2(0.53)Ga2(0.32)Al(0.15)As:Si	10.61min	207.82nm		LM
In12As(0.0051)P :Si	32.32min	513.61nm	3e17	
In2As(0.0113)P buffer:Si	34.32min	450.15nm	1e18	
InP (S-doped)				

VA163 In(0.76)GaAs laser 3QWs 492C

To grow a 1.95um laser with 3 In0.76GaAs QWs
Corresponding PL structure is VA161; Corresponding Laser Structures are VA162 (1.95um), VA150 and VA152 (1.55um), VA153 and VA154 (1.75um) and VA158 and VA159 (1.85um)
2 wafers grown; one is to be shipped to Covega for Processing

Layer	Time	Thickness	Doping	Strain
In1(0.53)Ga1As:Be	12.22min	100nm	3e19	LM
In12P:Be	34.1min	500nm	1e18 =>1e19	
In12P:Be	102.29min	1500nm	1e18	
In2(0.53)Ga2(0.313)Al(0.156)As:Be	1.057min	20nm	1e18	LM
In1P:Be	10.23min	150nm	3e17	
In2(0.53)Ga2(0.313)Al(0.156)As	9.51min	180nm		LM
In2(0.53)Ga2(0.313)Al(0.156)As	1.057min	20nm		LM
In12(0.7)Ga1As	0.439min	8nm		1.16%CS
In2(0.53)Ga2(0.313)Al(0.156)As	1.057min	20nm		LM
In12(0.7)Ga1As	0.439min	8nm		1.16%CS
In2(0.53)Ga2(0.313)Al(0.156)As	1.057min	20nm		LM
In12(0.7)Ga1As	0.439min	8nm		1.16%CS
In2(0.53)Ga2(0.313)Al(0.156)As:Si	10.567min	200nm		LM
In1P :Si	34.1min	500nm	3e17	
In1P buffer:Si	34.1min	500nm	1e18	
InP (S-doped)				

VA163 In(0.76)GaAs laser 3QWs 492C

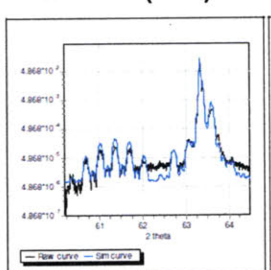

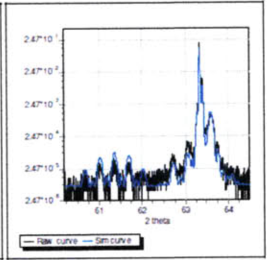

BEP_In1	2.49E-07 Torr
BEP_In2	2.53E-07 Torr
BEP_Ga1	1.75E-07 Torr
BEP_Ga2	2.04E-07 Torr
BEP_Al	0.33E-07 Torr
BEP_As/Valve_As	114E-07/280
BEP_P/Valve_P	118E-07/297
T_sub/DRS	590C/492C

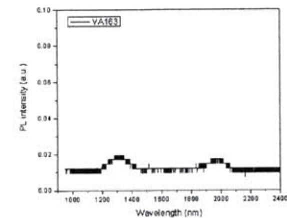

VA163 In(0.70)GaAs laser 3QWs 492C

Layer	Time	Thickness	Doping	Strain
In1(0.556)Ga1As(0.89)P:Be	12.22min	91.5nm	3e19	0.19%TS
In12As(0.00135)P:Be	34.1min	524nm	1e18 =>1e19	
In12As(0.0008)P:Be	102.29min	1476nm	1e18	
In2Ga2(0.357)Al(0.13)As:Be	1.057min	16.5nm	1e18	0.11%TS
In1As(0.0127)P:Be	10.23min	142.65nm	3e17	
In2Ga2(0.323)Al(0.156)As	9.51min	178.11nm		0.05%CS
In2Ga2(0.32)Al(0.16)As	1.057min	20.57nm		0.06%TS
In12(0.75)Ga1As	0.439min	9.63nm		1.5%CS
In2Ga2(0.32)Al(0.16)As	1.057min	20.57nm		0.06%TS
In12(0.75)Ga1As	0.439min	9.63nm		1.5%CS
In2Ga2(0.32)Al(0.16)As	1.057min	20.57nm		0.06%TS
In12(0.75)Ga1As	0.439min	9.63nm		1.5%CS
In2Ga2(0.32)Al(0.16)As:Si	10.567min	220.8nm		0.06%TS
In12P :Si	34.1min	521.7nm	3e17	
In1As(0.0052)P buffer:Si	34.1min	488.2nm	1e18	
InP (S-doped)				

Appendix B

Refractive Index

Layer	n	ref.	Thickness
$In_{0.53}Ga_{0.47}As$	3.43	[35]	100 nm
InP	3.132	[36]	2200 nm
$In_{0.48}Ga_{0.42}Al_{0.1}As$	3.42	[37]	20 nm
InP	3.132		50 nm
$In_{0.48}Ga_{0.42}Al_{0.1}As$	3.42		200 nm
$In_{0.85}Ga_{0.15}As$	3.486	[38]	8 nm
$In_{0.48}Ga_{0.42}Al_{0.1}As$	3.42		20 nm
$In_{0.85}Ga_{0.15}As$	3.486		80 nm
$In_{0.48}Ga_{0.42}Al_{0.1}As$	3.42		200 nm
InP	3.132		500 nm
InP	3.132		350 μm

Table B.1: Refractive index used for optical mode simulation

Appendix C

L-I-V

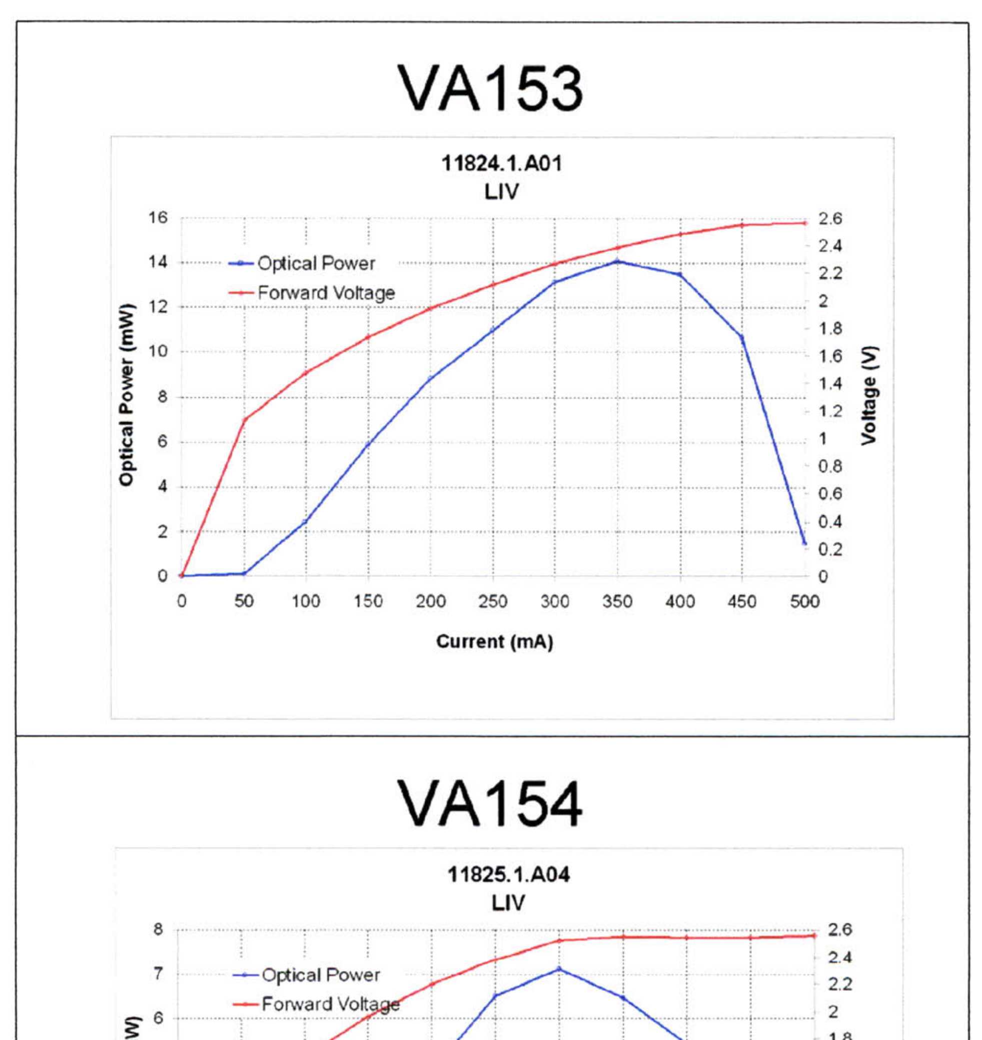
VA153
11824.1.A01
LIV
Optical Power
Forward Voltage
Optical Power (mW)
Voltage (V)
Current (mA)
0
2
4
6
8
10
12
14
16
0
0.2
0.4
0.6
0.8
1
1.2
1.4
1.6
1.8
2
2.2
2.4
2.6
0
50
100
150
200
250
300
350
400
450
500
VA154
11825.1.A04
LIV
Optical Power
Forward Voltage
Optical Power (mW)
Voltage (V)
Current (mA)
0
1
2
3
4
5
6
7
8
0
0.2
0.4
0.6
0.8
1
1.2
1.4
1.6
1.8
2
2.2
2.4
2.6
0
50
100
150
200
250
300
350
400
450
500

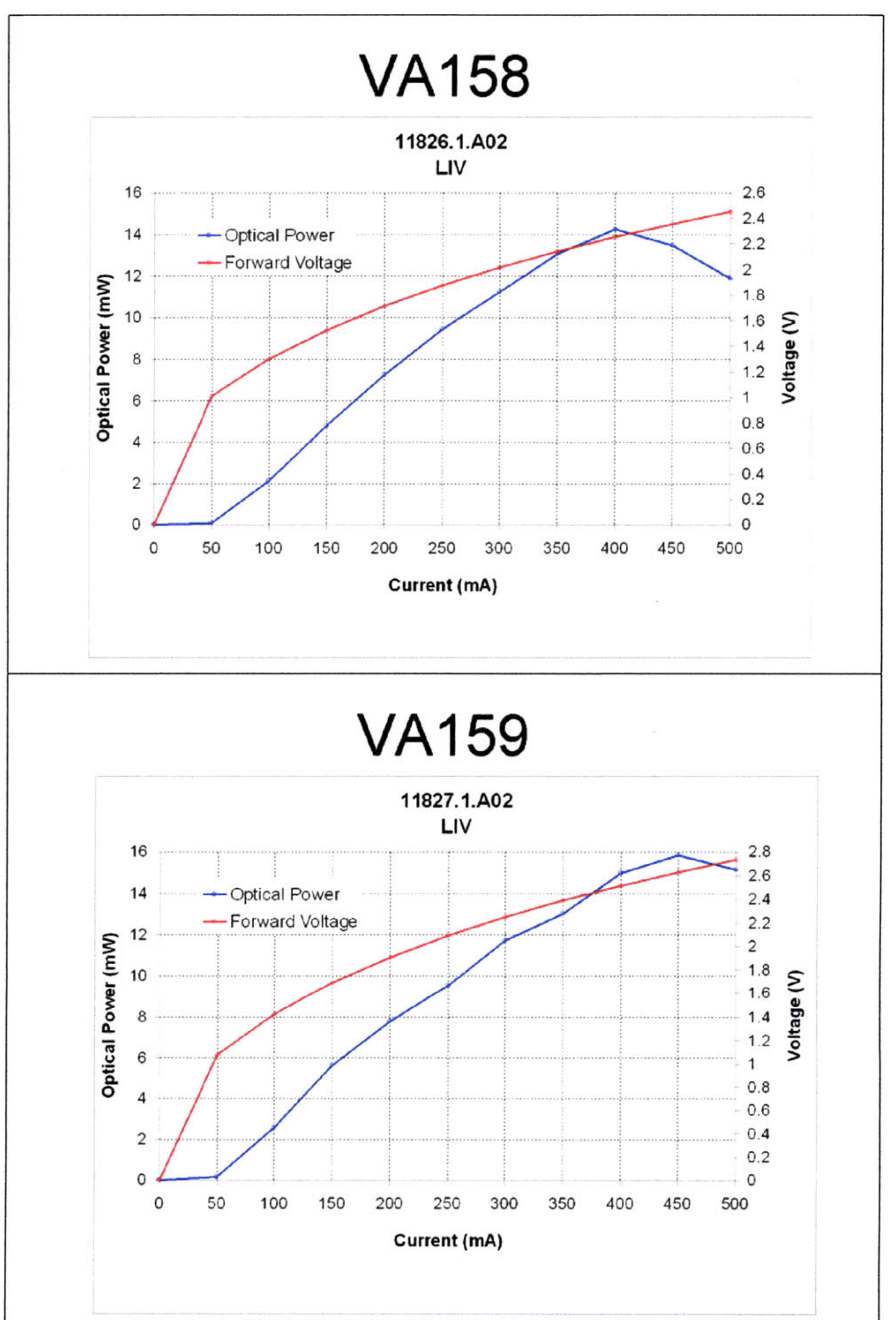
VA158
11826.1.A02
LIV
Optical Power
Forward Voltage
Optical Power (mW)
Voltage (V)
Current (mA)
VA159
11827.1.A02
LIV
Optical Power
Forward Voltage
Optical Power (mW)
Voltage (V)
Current (mA)

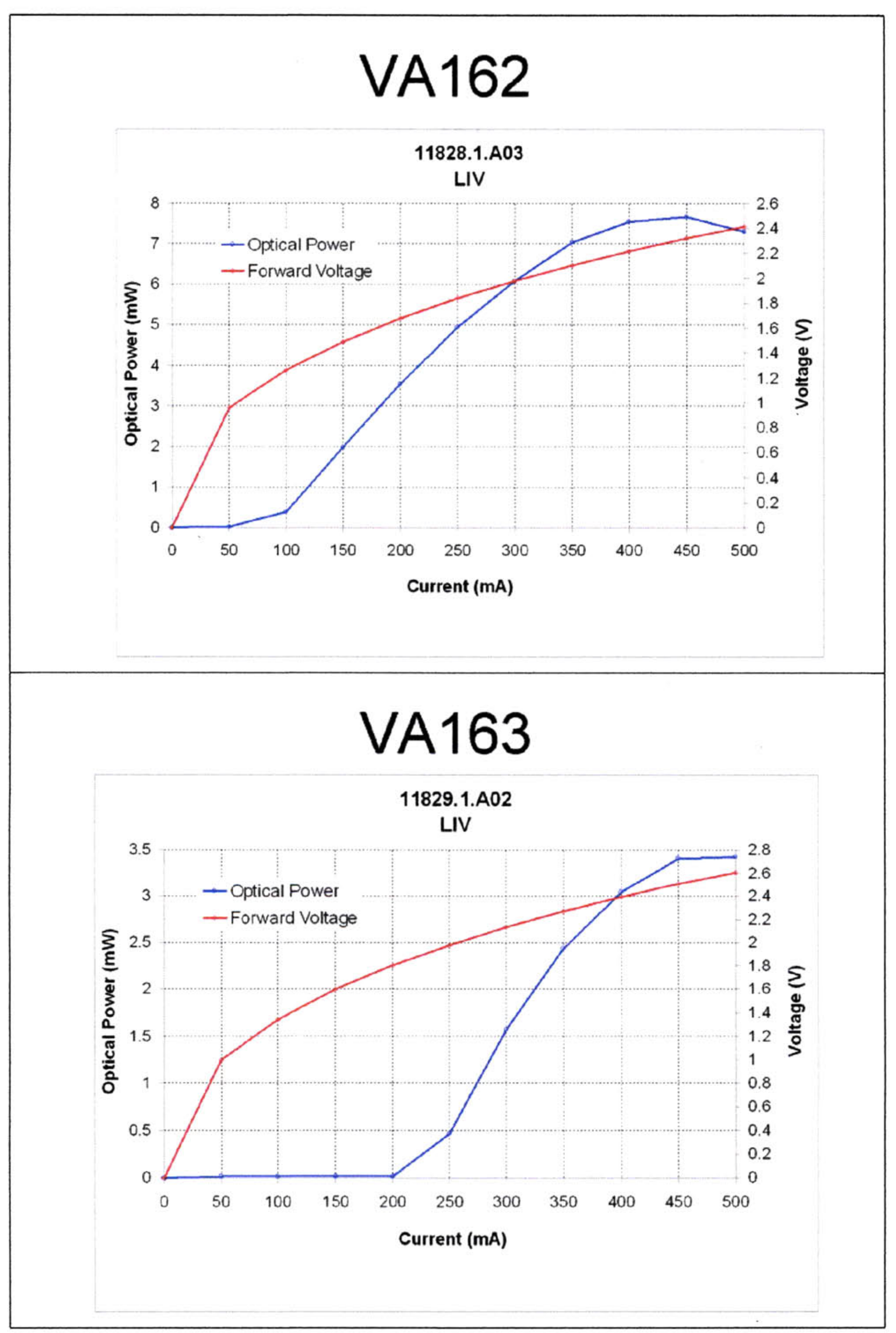
VA162
11828.1.A03
LIV
Optical Power
Forward Voltage
Optical Power (mW)
Voltage (V)
Current (mA)
VA163
11829.1.A02
LIV
Optical Power
Forward Voltage
Optical Power (mW)
Voltage (V)
Current (mA)

References

[1] L. A. Corzine and S. W. Corzine. *Diode Laser and Photonic Integrated Circuits.* Wiley-Interscience, 1995.

[2] Hong K. Choi. *Long-Wavelength Infrared Semiconductor Lasers.* Wiley Series in Laser and Applications, 2003.

[3] A. Krier. *Mid-Infrared Semiconductor Optoelectronics.* Springer, 2006.

[4] Us national institute of standards and technology. http://www.nist.gov.

[5] A. Rakovska, V. Berger, X. Marcadet, B. Vinter, K. Bouzehouane, and D. Kaplan. Optical characterization and room temperature lifetime measurements of high quality MBE-grown InAsSb on GaSb . *Semicond. Sci. Technol.*, 15:34, 2000.

[6] G. W. Turner, H. K. Choi, and M. J. Manfra. Ultralow-threshold (50A/cm^2) strained single-quantum-well GaInAsSb/AlGaAsSb lasers emitting at 2.05 μm. *Applied Physics Letters*, 72:876, 1998.

[7] Joachim Piprek, J. Kenton White, and Anthony J. What Limits the Maximum Output Power of Long-Wavelength AlGaInAs-InP Laser diodes? *Journal of Quantum Electronics*, 38:1253–1259, 2002.

[8] G. K. Kuang, G. Bohm, N. Graf, M. Grau, G. Rosel, R. Meyer, and M. C. Amann. Long wavelength InGaAs-InGaAlAs-lnP diode lasers grown by solid-source molecular-beam epitaxy . *Journal of Crystal Growth*, 227:334–337, 2001.

[9] C. G. Van de Walle. Band lineups and deformation potentials in the model-solid theory. *Phys. Rev. B*, 39:1871, 1989.

[10] M P C M Krijn. Heterojunction band offsets and effective masses in III-V quaternary alloys. *Semicond. Sci. Technol.*, 6:27–31, 1991.

[11] I. Vurgaftman and J. R. Meyer. Band parameters for III-V compound semiconductors and their alloys. *J. Appl. Phys.*, 89(11):5815–5875, 2001.

[12] R. People and J. C. Bean. Calculation of critical layer thickness versus lattice mismatch for Ge_xSi_{1-x}/Si strained-layer heterostructures. *Appl. Phys. Lett.*, 47:322, 1985.

[13] J. W. Matthews and A. E. Blakeslee. Defects in epitaxial multilayers: I. Misfit dislocations. *Journal of Crystal Growth*, 27:118, 1974.

[14] Harold by photon design. http;//www.photond.com/products/Harold.htm.

[15] M. O. Manasreh. *Antimonide-related strained-layer heterostructures.* Gordon and Breach, 1997.

[16] Leptos, bruker axs. http://www.bruker-axs.de/stress.html.

[17] Stephen J. Pearton, Paul H. Holloway, and Gary E. McGuire. *Hand Book of Compound Semiconductors, Ch8 Wet and Dry Etching of compound semiconductors,*. Noyes publications, 1995.

[18] Yan He, B. W. Liang, N. C. Tien, and C. W. Tu. Selective Chemical Etching of InP Over InAlAs. *Journal of Electrochemistry Society*, 139:2046, 1992.

[19] C. H. Henry, R. A. Logan, F. R. Merritt, and J. P. Luongo. The effect of intervalence band absorption on the thermal behavior of InGaAsP lasers. *IEEE Journal of Quantum Electronics*, QE-19, No.6:948, 1983.

[20] C. Lin, M. Gran, O. Dier, and M. C. Amann. Low threshold room-temperature continuous-wave operation of 2.24∼3.04μm GaInAsSb/AlGaAsSb quantum-well lasers. *Applied Physics Letters*, 84:5088, 2004.

[21] W. W. Bewley, I. Vurgaftman, C. S. Kim, M. Kim, C. L. Canedy, J. R. Meyer, J. D. Bruno, and F. J. Towner. Room-temperature "W" diode lasers emitting at λ∼4.0 μm. *Appl. Phys. Lett.*, 85:5544, 2004.

[22] C. Becker, I. Prevot, X. Marcadet, B. Vinter, and C. Sirtori. InAs/AlSb quantum-cascade light-emitting devices in the 3∼5 μm wavelength region. *Appl. Phys. Lett.*, 78:1029, 2001.

[23] Rui Q. Yang and S. S. Pei. Novel type II quantum cascade lasers. *J. Appl. Phys.*, 79:8197, 1996.

[24] L. A. Coldren and T. L. Koch. Analysis and design of coupled-cavity lasers-Part I: Threshold gain analysis and design guidelines. *IEEE J. Quantum Electron.*, 20:659, 1984.

[25] Muller M., Bauer A., Lehnhardt T., and Forchel A. Widely Tunable Photonic Crystal Coupled Cavity Lasers on GaSb. *IEEE Photonics Tech. Letts.*, 20:1100 – 1102, 2008.

[26] Romain Brenot, Odile Le Gouezigou, Francis Poingt, Fradric Pommereau, Lionel Le Gouezigou, Estelle Derouin, Olivier Drisse, François Lelarge, Hlne Sillard-Debrgeas, and Guang-Hua Duan. Widely Tunable Photonic Crystal Lasers. *Japanese journal of applied physics*, 46:7741, 2007.

[27] A. Bauer, M. Miller, T. Lehnhardt, K. Rner, M. Hemmer, and A. Forchel. GaSb-based lasers with two-dimensional photonic crystal mirrors . *Nanotechnology*, 19:15203, 2008.

[28] M. Kamp, H. Scherer, C. Ulzhifer, B. Vilker, A. Forchel, K. Janiak, H. Heidrich, R. Brnot, and G. H. Duan. Tunable photonic crystal laser with integrated wavelength monitor. In *European Conf. Optical Communication (ECOC) Paper Tu3.4.2.*

[29] M. Kondow, K. Uoni, A. Niwa, T. Kitatani, S. Watahiki, and Y. Yazava. GaIn-NAs: A Novel Material for Long-Wavelength-Range Laser Diodes with Excellent High-Temperature Performance. *Jpn. J. Appl. Phys.*, 35:1273, 1996.

[30] D. K. Shih, H. H. Lin, L. W. Sung, T. Y. Chu, and T. R. Yang. Band gap reduction in InAsN alloys. *Jpn. J. Appl. Phys.*, 42:375, 1996.

[31] I. Vurgaftman, J. R. Meyer, N. Tansu, and L. J. Mawst. Type-II "W" Quantum-Well Lasers. *J. Appl. Phys.*, 96:4653–4655, 2004.

[32] S. Ridene, M. Debbichi, H. Bouchriha, A. Ben Fredj, M. Said, J. L. Lazzari, Y. Cuminal, and P. Christol. A theoretical study of laser structures based on diluted nitide InAsN for mid-infrared operation. *Semiconductor Science and Technology*, 24:085010, 2009.

[33] M. Debbichi, A. Ben Fredj, Y. Cuminal, J. L. Lazzari, S. Ridene, H. Bouchriha, and P. Christol. InAsN/GaSb/InAsN "W" quantum well laser for mid-infrared emission: from electronic structure to threshold current density calculations. *Journal of Applied Physics*, 41:215106, 2008.

[34] James S. Harris. (GaIn)(NAsSb): MBE Growth, Heterostructure and Nanophotonic Devices. *International Journal of Nanoscience*, 6:269–274, 2007.

[35] Linnik M. and A. Christou. Calculations of Optical Properties for Quanternary III-V Semiconductor Alloys in the Transparent Region and Above (0.2∼4.0 eV). *Physica B*, 318:140–161, 2002.

[36] Ioffe physical technical institute. http://www.ioffe.ru/SVA/NSM/nk/A3B5/Gif/inp.gif.

[37] M. J. Mondry, D. I. Babic, J. E. Bowers, and L. A. Coldern. Refractive index of (Al,Ga,In)As Epilayers on InP for optoelectronic applications. *IEEE Photon. Technol. Lett.*, 4:627–630, 1992.

[38] Goldberg Yu. A., N. M. Schmidt, M. Levinshtein, S. Rumyantsev, and M. Shur. *Handbook Series on Semiconductor Parameters Vol.2* . World Scientific, London, 1999.